Li, C.-F., Lin, J., Kulhanek, D.K., and the Expedition 349 Scientists, 2015
Proceedings of the International Ocean Discovery Program Volume 349
publications.iodp.org

doi:10.14379/iodp.proc.349.106.2015

Site U1434[1]

C.-F. Li, J. Lin, D.K. Kulhanek, T. Williams, R. Bao, A. Briais, E.A. Brown, Y. Chen, P.D. Clift, F.S. Colwell, K.A. Dadd, W.-W. Ding, I. Hernández-Almeida, X.-L. Huang, S. Hyun, T. Jiang, A.A.P. Koppers, Q. Li, C. Liu, Q. Liu, Z. Liu, R.H. Nagai, A. Peleo-Alampay, X. Su, Z. Sun, M.L.G. Tejada, H.S. Trinh, Y.-C. Yeh, C. Zhang, F. Zhang, G.-L. Zhang, and X. Zhao[2]

Keywords: International Ocean Discovery Program, IODP, *JOIDES Resolution*, Expedition 349, Site U1434, South China Sea, pelagic red clay, nannofossils, seamount volcaniclastics, Ar-Ar dating, mid-ocean-ridge basalt, calcite compensation depth, basalt alteration, seafloor spreading, cooling effect, gravity flow deposit

Contents

Background and objectives

Site U1434 (proposed Site SCS-4E) is located about 40 km northwest of Site U1433 and is directly on the uplifted shoulder of the relict spreading center in the Southwest Subbasin (Figures **F1, F2, F3**). This site is also located just south of a large seamount that formed near the relict spreading center after the termination of seafloor spreading. During coring at Site U1433, we decided to use some of our remaining time to core at a second site in the Southwest Subbasin to obtain basement samples more proximal to the extinct spreading center. Site U1434 also offered the opportunity to sample volcaniclastic material from the nearby seamount, which can be compared to the seamounts located near Site U1431 in the East Subbasin.

Sites U1434 and U1433 form a short sampling transect in the Southwest Subbasin (see Figure **F7** in the Expedition 349 summary chapter [Li et al., 2015a]), and with age control from these two sites, the evolution of the Southwest Subbasin can be better understood. Coring at these sites should help to explain the sharp differences in magnetic amplitude between the East and Southwest Subbasins and test the existing opening models for the Southwest Subbasin (e.g., Pautot et al., 1986). Coring will help determine the age of this subbasin near the end of spreading and allow for correlation of ages from magnetic anomalies with biostratigraphic, magnetostratigraphic, and radiometric ages. The apparent weak magnetization in basement rocks (Li et al., 2008) will be examined through petrological analyses of chemical compositions and measurements of magnetic susceptibility. Rock samples cored here will place constraints on mantle evolution and oceanic crustal accretion, terminal processes of seafloor spreading, and the timing and episodes of postspreading seamount volcanism at the relict spreading center.

Operations

Site U1434 was an alternate site that was originally planned to core from the seafloor with the advanced piston corer/extended core barrel (APC/XCB) systems to refusal, drop a free-fall funnel, change to the rotary core barrel (RCB), and then core 100 m into basement. Because of time considerations, the plan was modified so that we drilled without coring to ~200 m below seafloor (mbsf) using the RCB and then cored into basement as deeply as time permitted. Logging would then be considered depending on hole depth and condition. Hole U1434A was drilled to 197.0 mbsf and then cored with the RCB (Table **T1**). Basement was encountered at ~280 mbsf, and the hole was advanced by rotary coring to a final depth of 312.5 mbsf. The hole was terminated because of poor hole conditions and poor recovery. In Hole U1434A, we drilled one interval of 197.0 m. The RCB was deployed 14 times, recovering 26.43 m of core over 115.5 m of penetration (22.9% recovery).

Transit to Site U1434

After an 18 nmi transit lasting 2 h, the vessel arrived at Site U1434 and switched into dynamic positioning mode at 0048 h (UTC + 8 h) on 20 March 2014. At 0110 h, an acoustic positioning beacon was deployed. The position reference was a combination of GPS signals and a single acoustic beacon.

Hole U1434A

An RCB bottom-hole assembly (BHA) was assembled with a new RCB C-7 bit. The core barrels were spaced out at the surface, and the 172.07 m BHA assembled. The BHA was lowered to 4000.9 m below rig floor (mbrf), and the top drive was picked up and spaced out to 4020.0 mbrf to spud Hole U1434A. A center bit

[1] Li, C.-F., Lin, J., Kulhanek, D.K., Williams, T., Bao, R., Briais, A., Brown, E.A., Chen, Y., Clift, P.D., Colwell, F.S., Dadd, K.A., Ding, W.-W., Hernández-Almeida, I., Huang, X.-L., Hyun, S., Jiang, T., Koppers, A.A.P., Li, Q., Liu, C., Liu, Q., Liu, Z., Nagai, R.H., Peleo-Alampay, A., Su, X., Sun, Z., Tejada, M.L.G., Trinh, H.S., Yeh, Y.-C., Zhang, C., Zhang, F., Zhang, G.-L., and Zhao, X., 2015. Site U1434. *In* Li, C.-F., Lin, J., Kulhanek, D.K., and the Expedition 349 Scientists, *Proceedings of the International Ocean Discovery Program, 349: South China Sea Tectonics:* College Station, TX (International Ocean Discovery Program). http://dx.doi.org/10.14379/iodp.proc.349.106.2015

[2] **Expedition 349 Scientists' addresses.**

MS 349-106: Published 30 March 2015

Figure F1. A. Bathymetric map of South China Sea region. Solid yellow circles = Expedition 349 sites. Pink circles = ODP Leg 184 sites. Yellow dashed line = inferred continent/ocean boundary, blue lines = fossil South China Sea spreading center, white flagged line = Manila Trench. B. Detailed bathymetry around Sites U1433 and U1434 (red box in A) showing nearby seamounts, Dangerous Grounds, and Reed Bank.

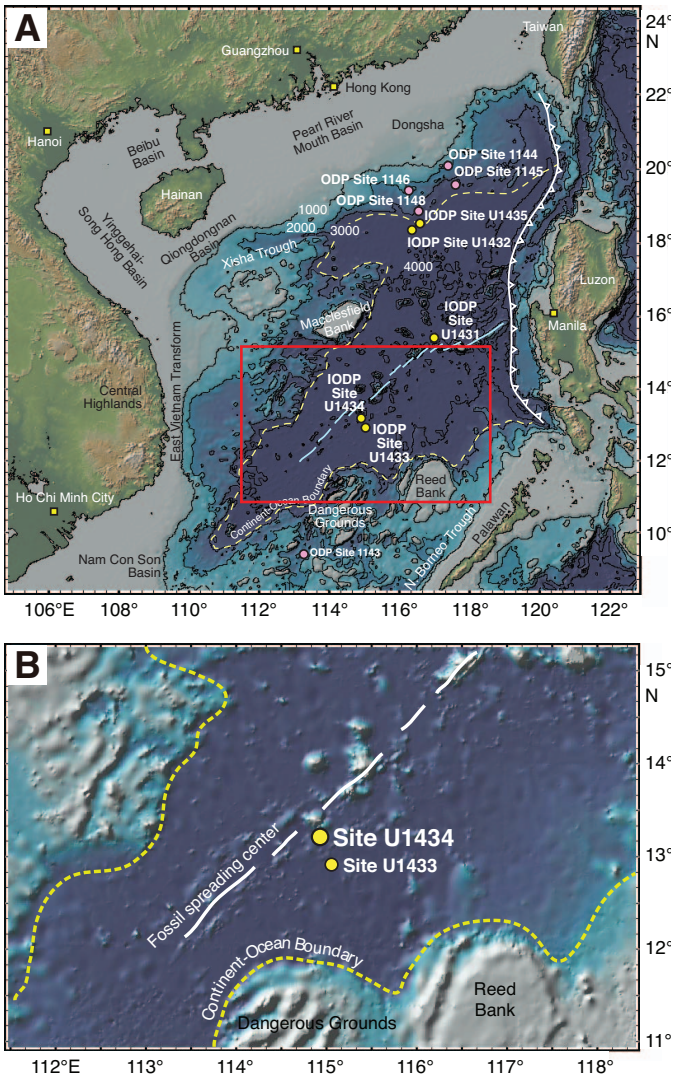

was dropped and pumped down the drill string to land out in the bit. Hole U1434A was spudded at 1215 h on 20 March 2014. The estimated depth of the seafloor was determined to be 4020.4 mbrf using the precision depth recorder. The final seafloor depth for the hole was 4020.4 mbrf (4009.0 m below sea level [mbsl]), which was determined by tagging the seafloor with the drill bit. Hole U1434A was advanced by drilling without coring from the seafloor to 4217.4 mbrf (197.0 mbsf) over a 10 h period. The center bit was then pulled, and a core barrel dropped to start continuous RCB coring from Core 349-U1434A-2R. Coring continued through Core 15R to a total depth of 4332.9 mbrf (312.5 mbsf). Microspheres were deployed in each RCB core catcher sub for the duration of RCB coring. We encountered the sediment/basement interface in Core 10R, with the formation change at ~280 mbsf. Coring continued into acoustic basement from Core 10R through 15R to a total depth of 4332.9 mbrf (312.5 mbsf). Half-cores were started with Core 12R and continued to total depth. Penetration rates varied

Figure F2. Magnetic anomalies near Sites U1433 and U1434 (data from Ishihara and Kisimoto, 1996). Bold black lines mark 3000 m isobaths outlining seamounts. Magnetic anomaly picks are from Briais et al. (1993).

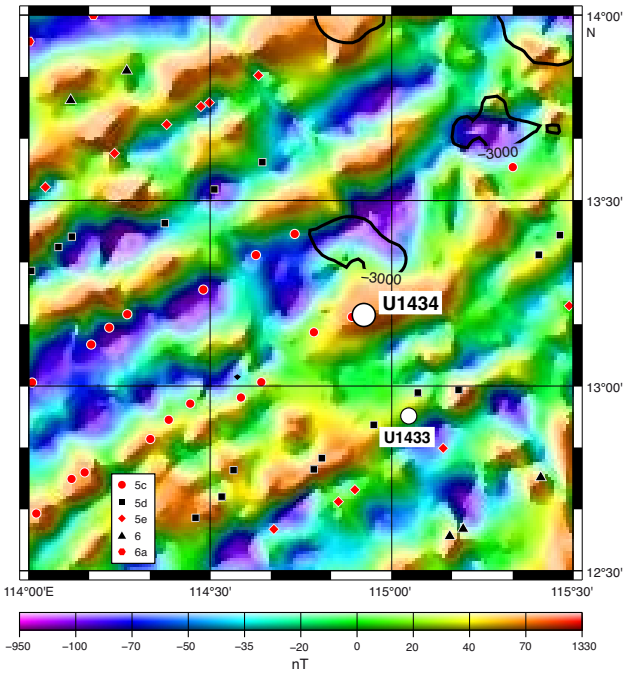

Figure F3. A. Regional bathymetric map showing seismic reflection profiles (red lines) and locations of Sites U1433 and U1434. Contour interval = 100 m. B. Seismic profile Line NDS3, with location of Site U1434. CPD = common depth point. Green line = interpreted top of basement.

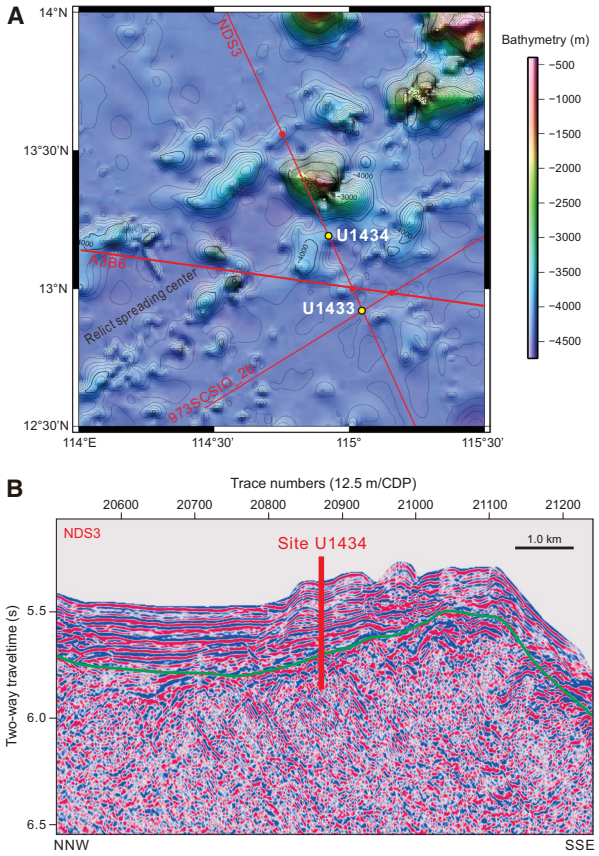

Table T1. Coring summary, Site U1434. CSF = core depth below seafloor, DRF = drilling depth below rig floor, DSF = drilling depth below seafloor. R = rotary core barrel, numeric core type = drilled interval. RCB = rotary core barrel. **Download table in .csv format.**

Hole U1434A
Latitude: 13°11.5080′N
Longitude: 114°55.4005′E
Water depth (m): 4009
Date started (UTC): 19 March 2014, 1648 h
Date finished (UTC): 22 March 2014, 1548 h
Time on hole (days): 3.0
Seafloor depth (m DRF): 4020.4
Seafloor depth calculation method: seafloor tag with drill bit
Rig floor to sea level (m): 11.40
Drilling System: 9-7/8 inch RCB bit with 172.07 m BHA
Penetration depth (mbsf): 312.50
Cored interval (m): 115.50
Recovered length (m): 26.43
Recovery (%): 23
Drilled interval (m): 197
Drilled interval (no.): 1
Total cores (no.): 14
RCB cores (no.): 14
Age of oldest sediment cored: middle Miocene

			Depth DSF (m)			Depth CSF (m)						
Core	Date (2014)	Time UTC (h)	Top of interval	Bottom of interval	Interval advanced (m)	Top of cored interval	Bottom of cored interval	Length of core recovered (m)	Length of core curated (m)	Recovery (%)	Sections (no.)	Comments
349-U1434A-												
11	20 Mar	1525	0	197.00	197.0	***Drilled from 0 to 197.0 m DSF without coring***						
2R	20 Mar	1630	197.00	206.00	9.0	197.00	197.55	0.55	0.55	6	2	Microspheres
3R	20 Mar	1830	206.00	215.70	9.7	206.00	209.27	3.27	3.27	34	4	Microspheres
4R	20 Mar	2020	215.70	225.40	9.7	215.70	216.49	0.79	0.79	8	2	Microspheres
5R	20 Mar	2145	225.40	235.10	9.7	225.40	225.82	0.42	0.42	4	1	Microspheres
6R	20 Mar	2320	235.10	244.80	9.7	235.10	239.72	4.62	4.62	48	4	Microspheres
7R	21 Mar	0050	244.80	254.50	9.7	244.80	247.23	2.43	2.43	25	3	Microspheres
8R	21 Mar	0220	254.50	264.20	9.7	254.50	258.82	4.32	4.32	45	4	Microspheres
9R	21 Mar	0350	264.20	273.90	9.7	264.20	266.71	2.51	2.51	26	3	Microspheres
10R	21 Mar	0610	273.90	283.60	9.7	273.90	278.46	4.56	4.56	47	5	Microspheres
11R	21 Mar	1405	283.60	293.30	9.7	283.60	284.63	0.82	1.03	8	1	Microspheres
12R	21 Mar	1620	293.30	298.10	4.8	293.30	293.95	0.46	0.65	10	1	Microspheres
13R	21 Mar	1910	298.10	302.90	4.8	298.10	298.85	0.47	0.75	10	1	Microspheres
14R	21 Mar	2320	302.90	307.70	4.8	302.90	303.56	0.5	0.66	10	1	Microspheres
15R	22 Mar	0220	307.70	312.50	4.8	307.70	308.65	0.71	0.95	15	1	Microspheres
				Total:	312.5			26.43	27.51	21	33	

from 1.57 to 5.76 m/h over the basement interval. Coring was finally halted because of poor core recovery coupled with high torque and poor coring conditions. The total depth of Hole U1434A was reached at 0925 h on 22 March. After reaching total depth, the final core was pulled to the surface and laid out. At the completion of coring Hole U1434A, 14 RCB cores had been cut over a 115.5 m interval, recovering 26.43 m of core (22.9% recovery).

After retrieving the final core, we attempted to pull the drill string from the hole; however, the high torque and high overpull made this impossible. After 1.5 h of working the pipe with a combination of high torque (900 A), overpull, and constant pumping action, the drill string came free and was pulled out of the hole with the top drive to 4117.4 mbrf (97.0 mbsf). The top drive was then set back, and the drill string was tripped to the surface. The bit cleared the seafloor at 1500 h and cleared the rotary table at 2300 h. After securing the rig floor for transit and pulling the hydrophones and thrusters, the vessel switched to cruise mode and began the transit to Site U1435 at 2348 h on 22 March. Total time spent in Hole U1434A was 71.0 h (3.0 days).

Lithostratigraphy

Lithostratigraphic units

Four lithostratigraphic units are defined within the cored sequence at Site U1434 based on a combination of visual core description and smear slide and thin section inspection as well as scanning for an array of physical properties, including magnetic susceptibility and color spectra (see **Lithostratigraphy** and **Physical properties** in the Methods chapter [Li et al., 2015b] for details). Three sedimentary units overlie a single igneous unit in the basaltic basement (Figures **F4, F5**). Unit I is composed of interbedded dark greenish gray claystone and black sandstone with occasional volcaniclastic breccia intervals. Unit II contains thick greenish gray nannofossil-rich claystone with very thin sandstone interbeds. Unit III dominantly consists of massive yellowish brown claystone with nannofossil- or foraminifer-rich claystone. This unit lies directly on the basaltic basement. Unit IV is discussed in detail in **Igneous petrology and alteration.**

Figure F4. Lithostratigraphy summary and interpretation of depositional processes, Site U1434.

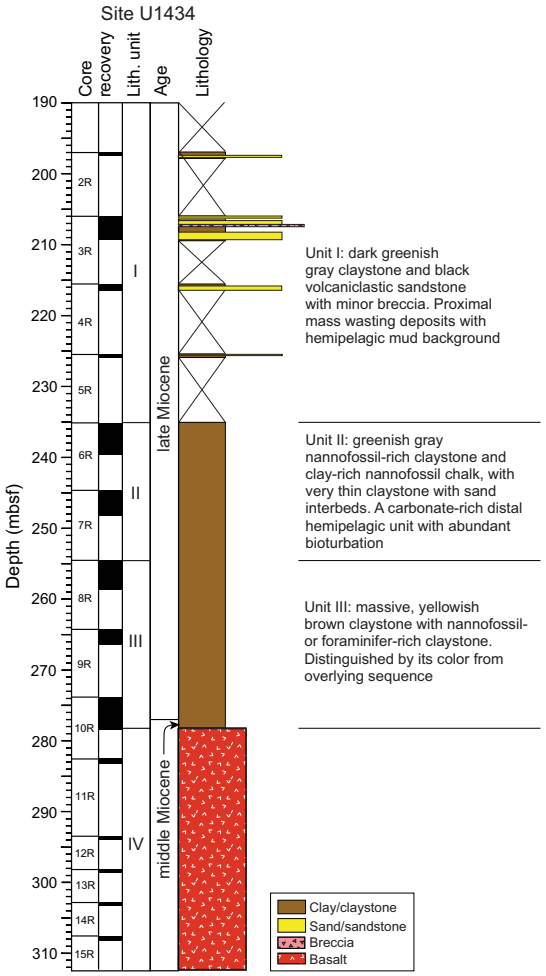

Figure F5. Correlation of lithostratigraphic units with magnetic susceptibility and reflectance spectroscopy data (after 20-point running average), Site U1434. Note the sharp increase in reflectance a* and b* at the Unit II/III boundary, which defines the transition.

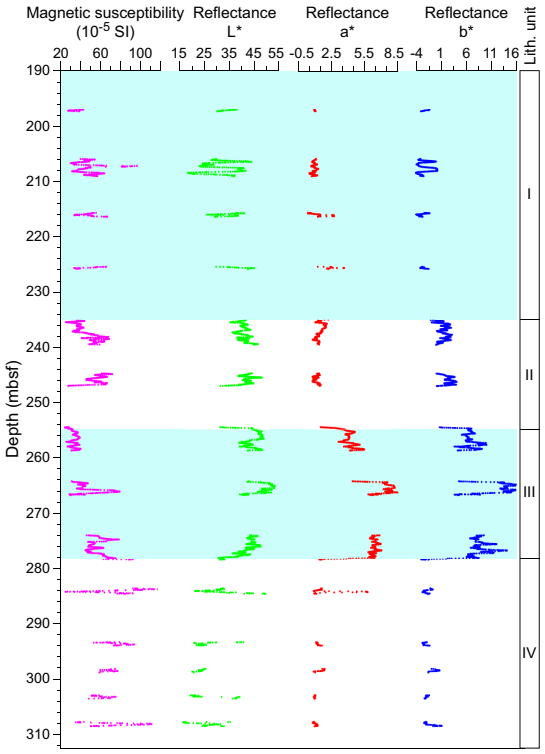

Figure F6. Volcaniclastic sandstone in Hole U1434A, Unit I. A. 3R-2A, 39–56 cm. B. 4R-1A, 17–32 cm.

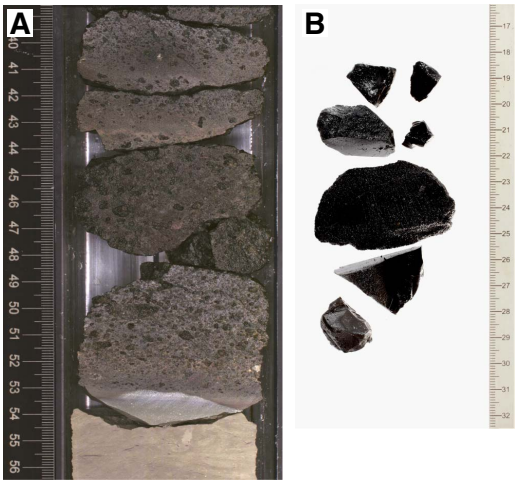

Unit descriptions

Unit I (197.00–235.10 mbsf)

Interval: 349-U1434A-2R-1, 0 cm, through 6R-1, 0 cm
Depth: 197.00–235.10 mbsf
Age: late Miocene

Unit I has extremely poor recovery in each core. Based on the recovered lithologies, we conclude that the unit is composed of interbedded claystone and sandstone with occasional volcaniclastic breccia intervals. Sandstone forms the majority of the recovered material (Figure F6). The claystone is mottled greenish and light buff brown with browner sediment preferentially found in burrows. The unit is marked by strong bioturbation within the claystone intervals that form ~40% of the total recovered sediment. The trace fossil assemblage in the claystone intervals is indicative of sedimentation in deep water (i.e., lower bathyal or abyssal depths, >2000 m), with assemblages dominated by *Chondrites* and *Zoophycos,* although vertical burrows are also noted.

Sandstone beds are typically dark gray or black and volcaniclastic in composition. They are interpreted to be relatively proximal deposits based on their medium- to coarse-sand grain size, and the presence of minor granule-sized breccia intervals. The grains are relatively angular and often moderately or even poorly sorted, especially at the base of clastic intervals. Sediment appears to have been transported by high-energy currents inferred from the observed parallel lamination within otherwise massive sandstone beds (Figure F7). More rarely, we observed ripple cross-lamination within coarse-grained, volcanic glass–rich sands that fine upward (Figure F8), indicative of a high-energy depositional environment. Some of the coarser intervals have a carbonate sand component, especially toward the base of the unit, although volcaniclastic material dominates the sand-sized fraction in the unit overall. Sandstone beds have sharp erosive bases and show poorly defined fining-upward se-

Figure F7. Gravity flow deposits in Hole U1434A, Unit I. A. Coarse-grained volcaniclastic sandstone and breccia (3R-1A, 5–22 cm). B. Graded sandstone with parallel and wavy laminations (3R-3A, 23–38 cm). C. Coarse-grained volcaniclastic sand grading upward into mottled greenish claystone with silt (4R-1A, 14–21 cm).

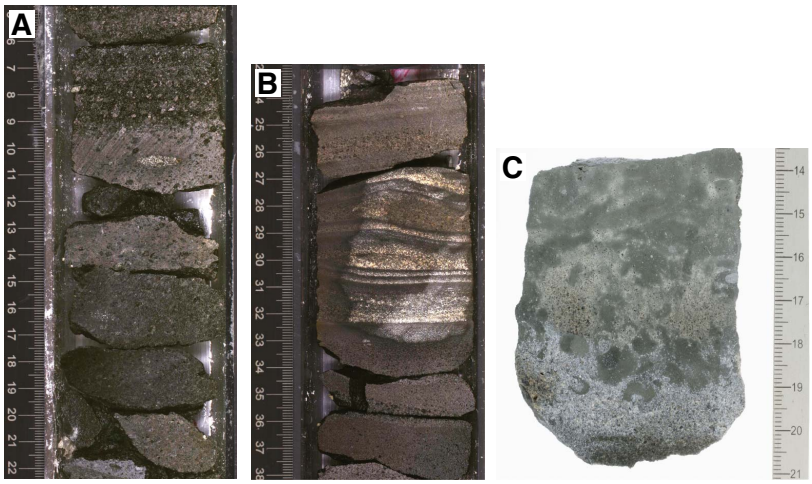

Figure F8. Laminated sandstone in Hole U1434A, Unit I, showing coarse-grained volcanic glass sands fining upward and with a sharp depositional base with the underlying fine-grained volcanic material (Sample 3R-3, 31 cm). A. Plane-polarized light (PPL). B. Cross-polarized light (XPL).

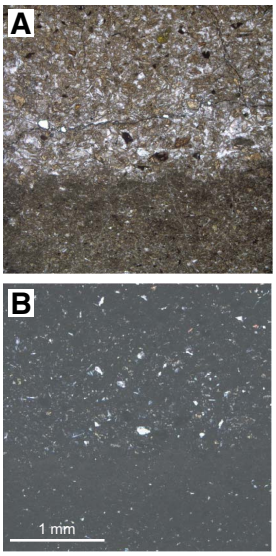

quences. Some of the beds have gradational upper contacts, passing uphole progressively into claystone intervals, although a minority of the sandstone intervals have sharp tops with a planar contact juxtaposing medium-grained sandstone directly with the overlying claystone.

We interpret the sandstone beds to be the product of gravity flow sedimentation during mass wasting. The claystone represents background hemipelagic sedimentation related to distal sediment flux. The lack of well-defined or expanded (>10 cm) graded tops indicates that there was little fine-grained material involved with these gravity flows. The common poor sorting of grains is suggestive of relatively rapid sedimentation close to the source, likely from a local volcanic edifice.

Unit II (235.10–254.59 mbsf)

Interval: 349-U1434A-6R-1, 0 cm, through 8R-1, 9 cm
Depth: 235.10–254.59 mbsf
Age: late Miocene

Unit II has better recovery and is finer grained than Unit I. The unit is dominated by nannofossil-rich claystone and nannofossil chalk with significant but variable quantities of clay. The color of the sediment varies at the decimeter scale as a result of the changing balance between carbonate and clay contents. The sediment is locally light greenish gray, reflecting higher biogenic carbonate content over those intervals. Bioturbation showing a typical deepwater assemblage is pervasive, and particularly visible in the interfaces between different sediment intervals. Compared to other ichnofacies seen in the Southwest Subbasin, we note fewer *Chondrites* and more large trace fossils, including *Planolites, Zoophycos,* and *Palaeophycus* (Figure **F9**), which are observed in present-day sediments in the South China Sea (Wetzel, 2009). The claystone is not purely composed of clay minerals and often contains fragments of volcanic glass, quartz silt, and large quantities of biogenic carbonate, largely in the form of nannofossils (Figure **F10**). Apart from bioturbation, the sediment is massive, suggesting no current influence during sedimentation. Although Unit II is distinguished from Unit I by its lack of significant sand content, we noted several very thin interbeds of graded claystone with sand that have erosive bases and gradational contacts with the overlying claystone. We interpret these intervals to be turbidites (Figure **F11**). These deposits are volumetrically insignificant. Overall, Unit II is more calcareous, more biogenic, and less siliciclastic than the overlying unit.

Unit III (254.59–278.27 mbsf)

Interval: 349-U1434A-8R-1, 9 cm, through 10R-CC, 13 cm
Depth: 254.59–278.27 mbsf
Age: latest middle to late Miocene

Unit III was recovered in three cores immediately overlying the basaltic basement. Like Unit II, this unit is dominated by fine-grained sediment, in particular claystone with variable amounts of

Figure F9. Nannofossil-rich claystone with heavy bioturbation in Hole U1434A, Unit II. Burrows are dominated by *Planolites, Palaeophycus,* and *Zoophycos.* A. Large vertical *Planolites* burrow (6R-1A, 4–22 cm). B. Inclined *Zoophycos* burrow (6R-1A, 44–59 cm). C. *Palaeophycus* burrows (7R-1A, 5–21 cm).

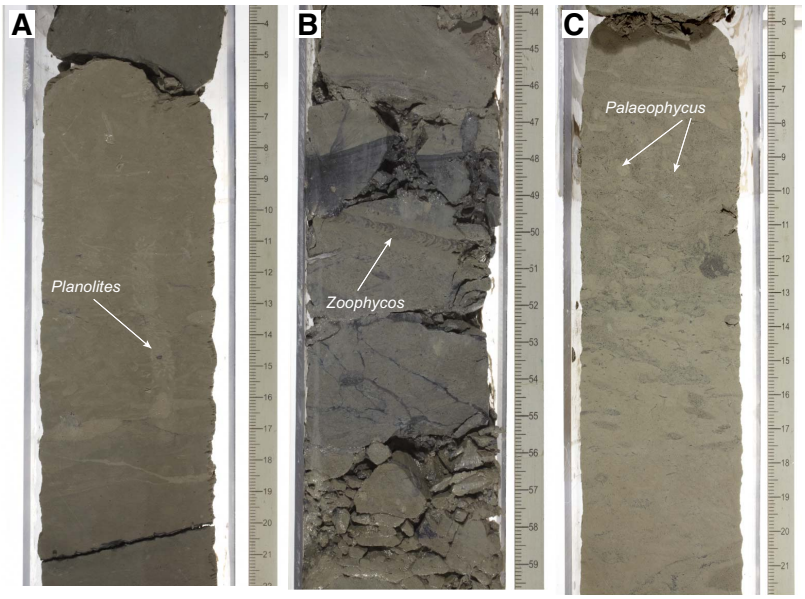

Figure F10. Typical nannofossil-rich claystone in Hole U1434A, Unit II (PPL). A. Nannofossil-rich claystone with minor quartz silt (6R-1A, 3 cm). B. Nannofossil-rich claystone with feldspar silt grain (7R-1A, 35 cm).

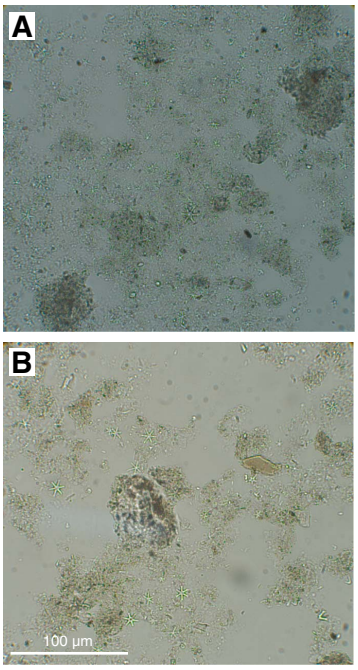

Figure F11. Very thin, dark sand layers with erosive bases, fining upward into carbonate-rich claystone in Hole U1434A, Unit II (6R-3A, (A) 16–26 cm, and (B) 91–102 cm.

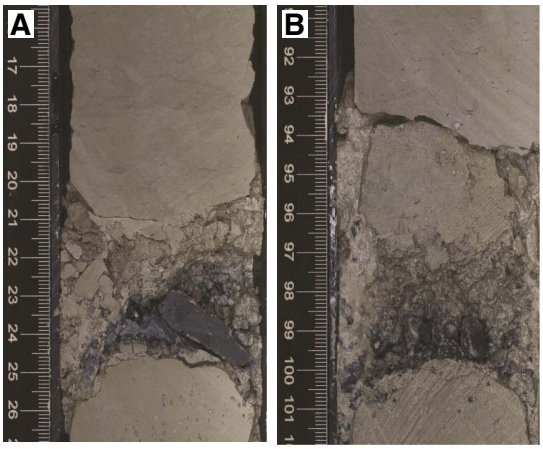

nannofossils that form the primary carbonate component in this sequence. This unit is primarily distinguished from Unit II by its color, which tends to be more yellowish or reddish brown compared to the greenish gray tones associated with the overlying unit (Figure **F12**). The claystone is especially saturated in dark yellowish brown tones in Core 349-U1434A-10R and becomes progressively lighter toward the unit top.

The boundary between this unit and the overlying Unit II is best observed in the color reflectance data (Figure **F5**) rather than in the lithology. As with Unit II, the sediment tends to be rather massive and structureless and shows very little evidence for current influence during sedimentation. The most obvious sedimentary structures are bioturbation features, which are relatively large and favor *Planolites* and vertical burrows rather than the delicate, branching *Chondrites* forms (Figure **F12**). At interval 349-U1434A-9R-1A, 13–16 cm, we identified a particularly large *Thalassionoides*-type burrow measuring 2.5 cm across. There is minor synsedimentary deformation in the form of faulting. Because some faults are small and do not cross the entire core, we suggest that movement occurred in a steep slope environment soon after the sediments had been consolidated (Figure **F13**). Foraminifers are clearly visible in this unit, especially in Core 349-U1434A-10R, where they are apparent on the

Figure F12. Burrows in yellowish brown claystone in Hole U1434A, Unit III. A. *Planolites* burrows (8R-2A, 0–18 cm). B. *Thalassionoides* and *Planolites* burrows (9R-1A, 6–22 cm).

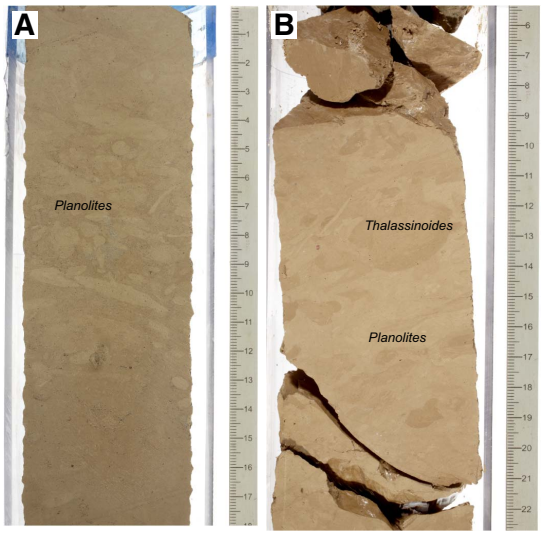

Figure F13. Small faults showing that tectonic activity affected Hole U1434A, Unit III. A. Small faults cutting burrows (9R-1A, 21–31 cm). B. Fault separating different colored claystone (10R-1A, 68–78 cm).

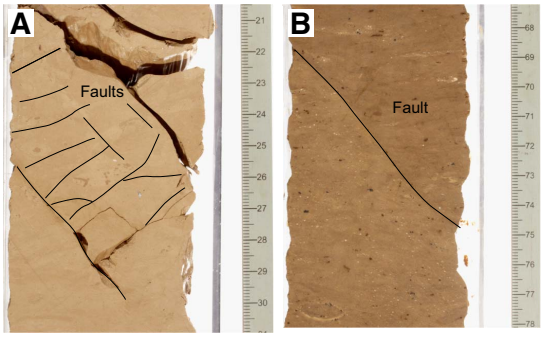

core surface as small white dots against the background of dark yellowish brown clay (Figure **F14**). In the lowermost 1 m of the unit are well-formed calcite crystals within an otherwise clay-rich sediment. These crystals do not show any evidence of having been redeposited or eroded and are assumed to have been recrystallized in situ. When these crystals are present, we see no other types of calcite of biogenic origin within the clay. Banding within the unit reflects variable amounts of carbonate versus pure clay material, which results in color variability. Typically, the different lithologies grade from one into the other with very little evidence of sharp or erosive boundaries within the unit; however, different-colored claystone intervals are juxtaposed across a fault at Section 349-U1434A-10R-1A, 71 cm (Figure **F13B**). The effects of diagenesis are visible in this unit, and are possibly caused by fluids derived from fluid-basalt interaction or by an increase in heat flow within the basin. The mottled yellowish brown and greenish claystone contains authigenic carbonate grains and abundant pyrite crystals (Figure **F15**).

We interpret Unit III to be largely the product of hemipelagic sedimentation with open-ocean biogenic carbonate mixing with distal clay derived from an adjacent continental margin, although exactly which landmass is the source of the clay is not apparent from

Figure F14. Yellowish brown claystone with planktonic foraminifers (10R-2A, 84 cm), showing well-preserved species of (a) *Dentoglobigerina altispira* and (b) *Globigerinoides sacculifer* (PPL).

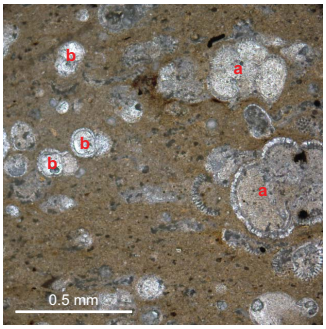

Figure F15. Yellowish brown and greenish mottled claystone, Hole U1434A (10R-3A, 45–64 cm). A. Mottled yellowish and greenish claystone with tiny pyrite microcrystals. B. Clay-sized grains with volcanic glass and plagioclase silt; authigenic carbonate occurs with the clay grains. Note the well-preserved planktonic foraminifer *Globigerinoides sacculifer* (PPL). C. Microcrystals of pyrite (10R-3, 53 cm) (reflected light).

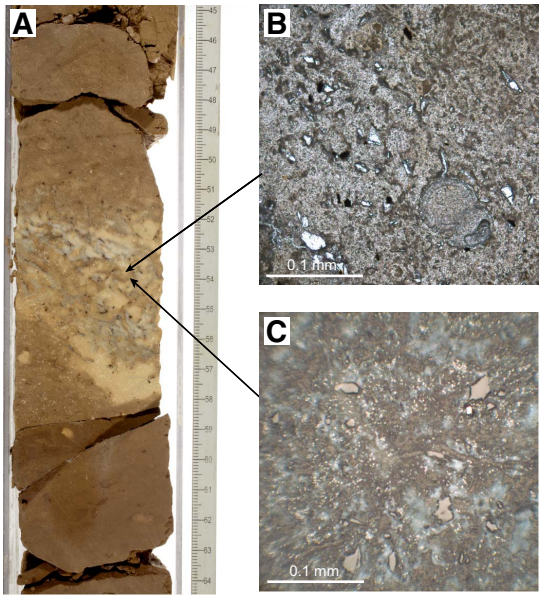

shipboard measurements alone. Strong current activity does not appear to have been important during the deposition of this unit, nor is there evidence to indicate hydrothermal influences or alteration after sedimentation beyond normal and rather mild degrees of burial diagenesis.

Discussion

Breccia and sandstone

The small amounts of breccia and black volcaniclastic sandstone in Unit I are in strong contrast to the clay and carbonate turbidite sediments recovered at Site U1433, which is located just ~35 km to the south. The coarse grain size and poor sorting indicate a relatively local provenance, and the volcanic character of the grains suggests the source is a volcanic edifice, most likely the adjacent seamount ~20 km to the north (Figures **F1, F3**). Based on the parallel lamination and erosive bases that are often associated with these deposits, the sediment was probably transported by gravity flow

currents, although some more localized mass wasting may be responsible for the less well sorted and coarser grained material.

Yellowish brown claystone

Like the other deepwater sites in the South China Sea basin drilled during Expedition 349, the volcanic basement at Site U1434 is covered by a deposit, ~25 m thick, of fine-grained reddish to yellowish brown claystone. The sediment is well consolidated but not entirely lithified, which is consistent with the relatively moderate depths of burial. The clay could be transported by hypopycnal plumes released from river mouths during periods of enhanced discharge, for example during heavy monsoon floods in Southeast Asia. The forcing of muddy megaturbidites from the neighboring continents by distal turbidity currents could be a mechanism of transportation (Wetzel and Unverricht, 2013). Mixture of this clay with significant amounts of biogenic carbonate suggests deposition at or above the calcite compensation depth.

Unlike for the relatively thick and common carbonate beds at Site U1433, which were interpreted as turbidites, we do not have evidence that the carbonate at Site U1434 is redeposited. Indeed, the well-formed, unbroken foraminifers seen within the claystone toward the base of Unit III are more suggestive of direct pelagic sedimentation without significant reworking, in contrast to the clay-rich siliciclastic component, which must be transported a long distance from the continental margin.

The location of the site on an uplifted and tilted footwall block of the oceanic basement is likely responsible for raising the subbasin in which Site U1434 was drilled above the abyssal seafloor and out of the path of many of the abyssal plain turbidites that we encountered at Site U1433. The relatively high elevation of the drill site area likely has resulted in a reduced flux of clastic turbidite muds to dilute the pelagic carbonate rain from the upper levels of the ocean. Pelagic carbonate microfossils preserved at this site indicate that it was located above the calcite compensation depth.

The reddish to yellowish brown color of much of Unit III is likely related to more enhanced oxidation of the clastic components of the sediment compared to the more rapidly deposited dark greenish gray claystone found at shallower levels at this site. Advanced oxidation of this type is typical in regions of slow sedimentation and oxygenated bottom water, and similar deposits are known throughout much of the Pacific away from the equatorial zone of enhanced biogenic production (Bryant and Bennet, 1988). The red clays at this site are thicker than might be expected from the Pacific analogs given their relative youth, but this may reflect the faster sediment supply linked to the relative proximity to continental sources.

Biostratigraphy

We analyzed all core catcher samples from Hole U1434A for calcareous nannofossils, planktonic foraminifers, and radiolarians. Calcareous nannofossils in selected split-core samples were also analyzed. Coring started at 197.0 mbsf at this site. Biostratigraphy based on calcareous nannofossils and planktonic foraminifers indicates that the sediment recovered at Site U1434 spans the uppermost middle to upper Miocene, with the base of the sequence younger than 11.9 Ma (Figure **F16;** Tables **T2, T3**). Calcareous nan-

Figure F16. Age-depth model, Site U1434. FAD = first appearance datum, FCA = first common appearance, LAD = last appearance datum.

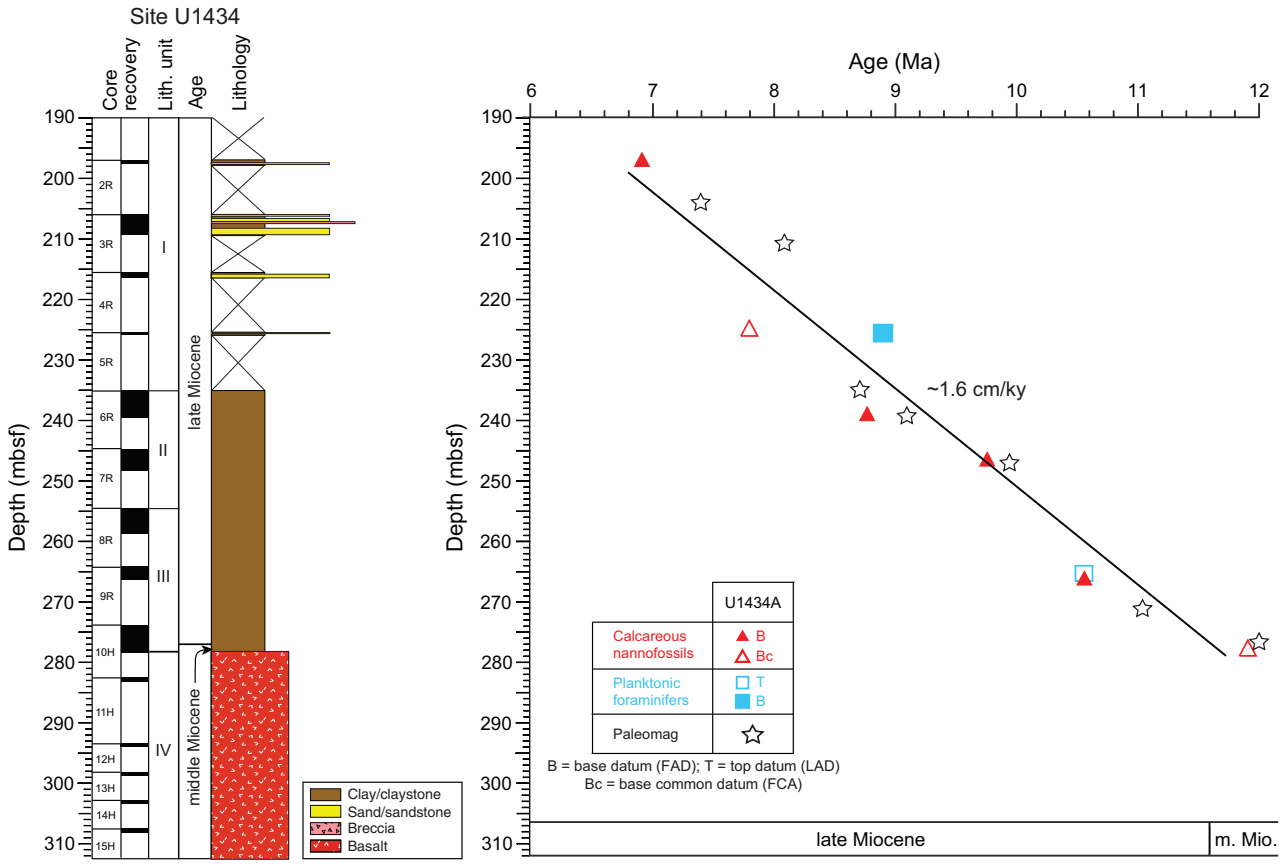

Table T2. Depths and ages of calcareous nannofossil events, Hole U1434A. T = top/last appearance datum, B = base/first appearance datum, Bc = base common/first common appearance. **Download table in .csv format.**

Epoch	Zone (Martini, 1971)	Calcareous nannofossil event	Hole U1434A Core, section, interval (cm)	Hole U1434A Top depth (mbsf)	Age (Ma)
late Miocene	NN11	B *Nicklithus amplificus*	2R-CC	197.47	6.91
		Bc *Discoaster surculus*	5R-CC	225.56	7.79
	NN10	B *Discoaster loeblichii*	6R-CC	239.62	8.77
	NN9	B *Minylitha convallis*	7R-CC	247.08	9.75
		B *Discoaster hamatus*	9R-CC	266.61	10.55
middle Miocene	NN7	Bc *Discoaster kugleri*	10R-CC, 14–16	278.28	<11.9

Table T3. Depths and ages of planktonic foraminifer events, Hole U1434A. T= top/last appearance datum, B = base/first appearance datum. **Download table in .csv format.**

Epoch	Zone (Berggren et al., 1995; Wade et al., 2011)	Planktonic foraminifer event	Hole U1434A Core, section	Hole U1434A Top depth (mbsf)	Age (Ma)
late Miocene	M13a	B *Globigerinoides extremus*	5R-CC	225.71	8.93
	M12/M11	T *Paragloborotalia mayeri*	9R-CC	266.61	10.46

Table T4. Distribution of calcareous nannofossils, Hole U1434A. **Download table in .csv format.**

Table T5. Distribution of planktonic foraminifers, Hole U1434A. **Download table in .csv format.**

Table T6. Distribution of radiolarians, Hole U1434A. **Download table in .csv format.**

nofossil age control is based on six bioevents; planktonic foraminifer age control is based on two bioevents and the overall assemblage.

Calcareous nannofossils are generally common to abundant with poor to moderate preservation, although the abundance decreases downhole (Table **T4**). Planktonic foraminifer abundance varies from common to barren, and preservation varies from good to poor with frequent observance of test fragmentation (Table **T5**). Radiolarians are absent in most samples, except for Sample 349-U1434A-8H-CC (258.56 mbsf), where a few well-preserved specimens are present (Table **T6**).

Correlation of microfossil biohorizons with paleomagnetic data suggests a sedimentation rate of ~1.6 cm/ky during the late middle to late Miocene at Site U1434 (Figure **F16**).

Calcareous nannofossils

Calcareous nannofossil biostratigraphy in Hole U1434A was established through analysis of core catcher and additional split core samples. Nannofossils are abundant to common in most samples but rare to absent in Samples 8R-CC (258.56 mbsf), 10R-CC (278.14 mbsf), and 10R-CC, 14–16 cm (278.28 mbsf). Preservation of nannofossils is poor to moderate (Table **T4**). Five late Miocene and one middle Miocene nannofossil bioevents indicate that the age of the sedimentary sequence is ~6.9 to <11.9 Ma (Table **T2;** Figure **F16**).

The presence of the first appearance datum (FAD) of *Nicklithus amplificus* (6.91 Ma) in Sample 349-U1434A-2R-CC (197.47 mbsf) and the first common appearance (FCA) of *Discoaster surculus* in Sample 5R-CC (225.56 mbsf) indicate Zone NN11. The FAD of *Discoaster berggrenii,* which marks the Zone NN11/NN10 boundary, is found in Sample 5R-1, 16-20 cm (225.56 mbsf). The FAD of *Discoaster loeblichii* (8.77 Ma) in Sample 6R-CC (239.62 mbsf) falls within Zone NN10, whereas the FAD of *Minylitha convallis* (9.75 Ma) in Sample 7R-CC (247.08 mbsf) occurs within Zone NN9, indicating that the Zone NN10/NN9 boundary occurs in Core 7R. The Zone NN9/NN8 boundary is assigned to Sample 9R-CC (266.61 mbsf) based on the FAD of *Discoaster hamatus* (10.55 Ma). The presence of *Cyclicargolithus floridanus* (LAD at 11.85 Ma) and *Discoaster kugleri* (FCA at 11.9 Ma) in Sample 10R-CC, 14–16 cm (278.28 mbsf) from the base of the brown claystone (lithostratigraphic Unit III) immediately overlying basalt, indicates an age <11.9 Ma for the base of the sediment section recovered at this site. The middle/late Miocene boundary is placed between Samples 9R-CC and 10R-CC (266.61 and 278.14 mbsf, respectively).

Planktonic foraminifers

Planktonic foraminifers were analyzed in core catcher samples from Hole U1434A. Foraminifer abundance varies from common to barren with good to poor preservation (Table **T5**). Recrystallization, partial dissolution, and fragmentation also occur, with fragments accounting for as much as 50% of the assemblage in Sample 9R-CC (266.61 mbsf), and heavy dissolution is evident in Samples 9R-CC (266.61 mbsf) and 10R-CC (278.14 mbsf). In these samples, the planktonic foraminifer assemblage is dominated by dissolution-resistant species such as *Sphaeroidinellopsis seminulina.*

The planktonic foraminifer assemblage includes species typical of the late Miocene, such as *Dentoglobigerina altispira, S. seminulina, Sphaeroidinellopsis kochi, Globoturborotalita nepenthes, Neogloboquadrina acostaensis,* and *Globorotalia limbata*. The planktonic foraminifer biostratigraphy for Hole U1434A is based on two bioevents, as well as the species composition of the planktonic foraminifer assemblage, which indicate late Miocene Zones M13–M11 (Table **T3;** Figure **F16**).

The absence of the dissolution-resistant species *Pulleniatina primalis* from the assemblage indicates an age >6.60 Ma (Subzone M13b) for the upper sedimentary sequence recovered in the hole. The FAD of *Globigerinoides extremus* (8.93 Ma) is observed in Sample 5R-CC (225.71 mbsf), indicating Subzone M13a. The Subzone M13a/Zone M12 boundary could not be identified because plank-

tonic foraminifers are either scarce or absent in Samples 6R-CC through 8R-CC (239.62–258.56 mbsf). The last appearance datum (LAD) of *Paragloborotalia mayeri* (10.46 Ma) in Sample 9R-CC (266.61 mbsf) indicates the Zone M12/M11 boundary. From the base of the sedimentary sequence, Sample 10R-CC (278.14 mbsf) also contains *P. mayeri* and other middle to late Miocene species, indicating Zone M11 (older than 10.46 Ma).

Radiolarians

In Hole U1434A, all core catchers are barren of radiolarians, except Sample 8H-CC (258.56 mbsf), which contains a few well-preserved specimens. However, this sample does not contain any marker species, although the presence of *Astrophacus* sp. indicates a biostratigraphic range between the middle Miocene and early Pliocene (Wang and Yang, 1992) (Table **T6**).

Igneous petrology and alteration

We cored 30.38 m into igneous basement below 278.27 mbsf in Hole U1434A and recovered 3.05 m of basalt (10.0% recovery). This short basement succession is divided into 7 igneous lithologic units, which are grouped into lithostratigraphic Unit IV (Figure **F17**). The basement at Site U1434 comprises a succession of small pillow basalt flows, or a single thicker autobrecciated pillow lava flow, with three occurrences of hyaloclastite breccia. The igneous basement is overlain by hemipelagic yellowish brown claystone (Unit III) that grades upward into nannofossil-rich claystone and chalk (Unit II) and a volcaniclastic series containing black volcaniclastic sandstone and minor breccia (Unit I). The latter volcaniclastic sandstone and breccia are interpreted to be part of the sedimentary apron of a nearby seamount, as they contain abundant volcanic glass fragments, scoria, and basalt clasts, as well as crystal fragments of plagioclase, olivine, and sparse biotite.

Figure F17. Lithostratigraphic summary of igneous rocks and lithologic features, Hole U1434A. Lithostratigraphy column includes lithology, igneous lithologic units (1–7), and lithostratigraphic units (I–IV). EOH = end of hole.

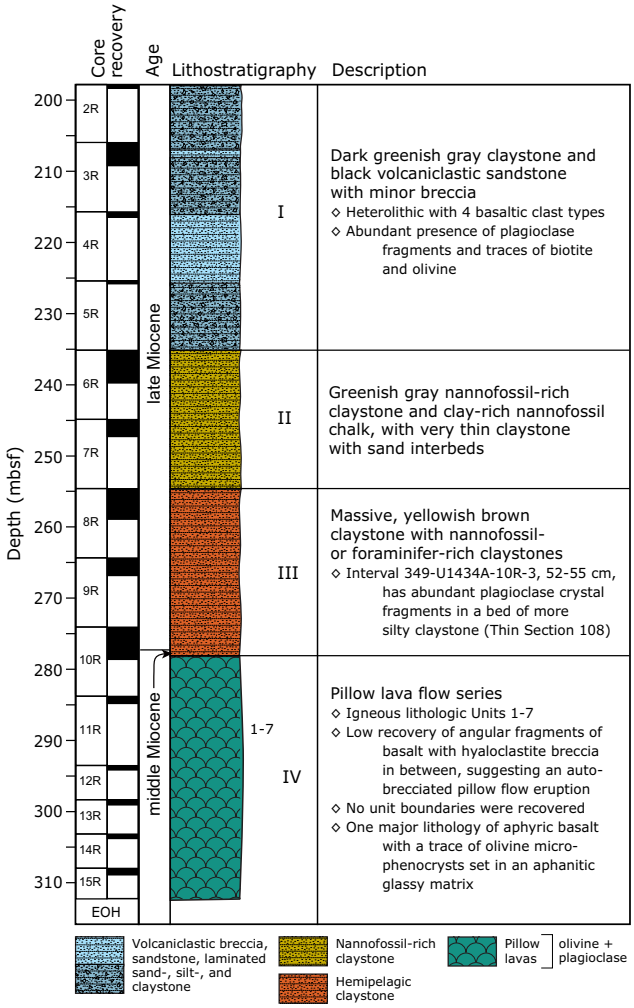

The igneous basement comprises angular to subangular basalt fragments that are aphyric and have glassy to microcrystalline groundmasses. The only phenocryst observed is olivine, which occurs as a sparse euhedral to subhedral equant mineral phase throughout the recovered igneous unit basement. The groundmass texture ranges from hypocrystalline to hypohyaline, mostly consisting of variably altered glass and mesostasis, but with abundant plagioclase microlites that grow in spherulitic and variolitic patterns. Clinopyroxene is only observed in a few thin sections in Cores 349-U1434A-13R through 15R, where it crystallized in small (<0.5–1 mm) patches, filling the interstitial spaces between plagioclase microlites in the groundmass. Most basalts are nonvesicular to sparsely vesicular. Chilled margins are mostly absent, although hyaloclastite breccia with abundant fresh volcanic glass shards set in a light brown carbonate and clay matrix is encountered in three intervals. Despite their cryptocrystalline and aphyric nature, all basalts have phase assemblages of olivine + plagioclase, with clinopyroxene as a sparse interstitial groundmass phase. These minerals are typical of mid-ocean-ridge basalt (MORB) crystallization assemblages and, in conjunction with geochemical evidence, we conclude that the basement basalt at Site U1434 is MORB (see **Geochemistry**).

Basalt alteration at Site U1434 is typical of that of MORB and ranges in intensity from slight to moderate. The majority of the pillow basalt pieces exhibit alteration halos with colors ranging from dark gray in their fresh interiors to light yellow-brown along the altered outer rims. More altered pieces are light gray with brown alteration tinges. Secondary minerals include a low-temperature alteration assemblage of clay, Fe oxide, carbonate, and celadonite. Fresh basaltic glass occurs in some of the pillow basalt margins and as clasts in the hyaloclastite breccia. Those basaltic glasses are partly altered to palagonite, ranging in color from orange to brown. Most vesicles are not filled or are partly filled with Fe oxide, saponite, celadonite, and carbonate. Alteration veins are uncommon in the recovered basement cores, with only two thin carbonate-filled veins recorded.

Lithostratigraphic Unit IV is devoid of seamount-derived volcanic products, but the cored sequence of volcaniclastic rocks in Unit I (and a single ~10 cm interbed in Unit III) probably originated from intraplate volcanism, as evidenced by plagioclase and biotite crystal fragments and high abundances of highly vesicular scoria, plagioclase-phyric and trachytic basalt clasts, and finer grained (fresh) volcanic glass shards in these intervals. As was the case for Site U1431, it is likely that we penetrated (partly) through the volcanic apron of the nearby seamount to the north (Figure **F1**), which must have been active during the late Miocene (see **Lithostratigraphy**).

Basaltic clasts in volcaniclastic Unit I

Lithostratigraphic Unit I contains a sequence of black volcaniclastic sandstone and minor breccia alternating with greenish gray

claystone. This late Miocene unit contains volcaniclastic sandy turbidites and may represent part of a seamount apron series (see **Lithostratigraphy**). All cored volcaniclastic breccias and sandstones are heterolithic and contain up to three basaltic clast types, as well as many broken pieces of primary volcanic crystal phases, including mainly plagioclase and olivine but also sparse biotite. Although Unit III comprises a yellowish brown claystone rich in nannofossils and foraminifers, it also contains a single bed with abundant plagioclase fragments. Each major basalt clast type and crystal fragment type (Figure **F18**) is described below from highest to lowest abundance in the section.

Type 1: nonvesicular basaltic glass shards

As one of the two major clast types, these Type 1 glass shards are angular to subangular, show minor feldspar laths, and are typically nonvesicular (Figures **F18A, F18B, F18D**). In many of the volcaniclastic breccias and sandstones, this clast type appears to be most common in the finer grain size fraction (Figure **F18D**).

Type 2: vesicular devitrified basaltic glass shards

As the other major clast type, these Type 2 glass shards or clasts are often scoriaceous with well-developed rounded vesicles clearly visible (Figure **F18A**). These clasts are angular to subangular, dark gray, and brown-gray when oxidized. Some clasts contain plagioclase microlites. All clasts are cryptocrystalline and seem to consist of completely devitrified volcanic glass.

Type 3: plagioclase and olivine crystal fragments

Throughout lithostratigraphic Unit I, plagioclase fragments (1%–2%) are up to 10 mm in size with generally sharp outlines (Figure **F18C**). These Type 3 plagioclase fragments are overall unaltered. Although plagioclase dominates the crystal fragments in the volcaniclastic sandstone and breccia, flakes of well-preserved biotite and crystal fragments of relatively unaltered olivine occur in many thin sections. The combined presence of plagioclase, olivine, biotite, and trachytic basalt points to an intraplate volcanic source, potentially the neighboring seamount near Site U1434 (Figures **F1, F3**).

Figure F18. Volcaniclastic sandstones and breccias, Hole U1434A, Unit I. A. Matrix-supported volcaniclastic sandstone with abundant devitrified (opaque) as well as fresh (brown) volcanic glass (gl) shards and a sparse trachytic basalt clast with plagioclase microlites (3R-2, 40–42 cm; TS103; PPL). carb = carbonate. B. Matrix-supported volcaniclastic sandstone with abundant fresh (brown) volcanic glass shards, containing olivine and plagioclase phenocrysts in a cryptocrystalline groundmass with plagioclase microlites (4R-1, 35–37 cm; TS 106; PPL). C. Plagioclase (plg) fragment in volcaniclastic sandstone (3R-2, 40–42 cm; TS103; XPL). D. Fine-grained laminated volcaniclastic sandstone with a black layer showing high proportions of basaltic glass shards, including plagioclase laths (3R-3, 28–32 cm; TS104; PPL).

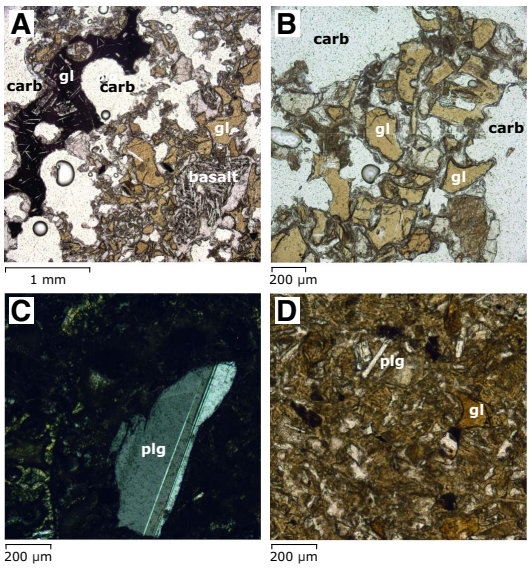

Type 4: trachytic basalt

This minor clast type is not easily observed macroscopically in the archive-half sections; however, it occurs in thin sections (Figure **F18A**). The clasts are subangular, small (up to 5 mm) and have a fine-grained groundmass with many flow-aligned plagioclase laths. These clasts are typically nonvesicular and slightly to moderately altered.

Lithostratigraphic and igneous lithologic units

Unit IV

Interval: 349-U1434A-10R-CC, 13 cm, to 15R-1, 95 cm
Depth: 278.27–308.65 mbsf
Thickness: 30.38 m (3.05 m at 10.0% recovery)
Lithology: pillow basalt flows with interspersed hyaloclastite breccia
Igneous lithologic units: 1–7

The base of the yellowish brown hemipelagic claystone (lithostratigraphic Unit III) and the first appearance of aphyric pillow basalt fragments in the lowermost 8 cm of the core catcher of Core 349-U1434A-10R mark the upper boundary of lithostratigraphic Unit IV at 278.27 mbsf (curated depth). Unit IV comprises blocky (small) pillow basalt fragments with three occurrences of hyaloclastite breccia in between (Figures **F19, F20, F21, F22**). All basalt samples are aphyric and have glassy to aphanitic groundmasses, with olivine being the singular phenocryst phase present (Figure **F22C**). The groundmass contains a high proportion of variably altered and devitrified glass and mesostasis, with plagioclase microlites forming typical spherulitic and variolitic textures (Figure **F22A, F22B, F22D**) indicative of relatively high cooling rates upon eruption. Clinopyroxene is only observed in a few thin sections, where it crystallized in patches (<0.5–1 mm) and fills interstitial spaces between plagioclase microlites (Figure **F22D**). Most basalts are nonvesicular to sparsely vesicular. Chilled margins are mostly absent, although in three intervals hyaloclastite breccias were encountered with shards of fresh volcanic glass (Figures **F21C, F21D**) or blocky aphyric basalt with chilled margins (Figure **F21A, F21B**) appearing in a carbonate and/or clayey matrix.

Igneous lithologic Units 1, 3, 5, and 7 are poorly recovered, and unit boundaries are inferred from the occurrence of chilled margins on separate angular basalt pieces and hyaloclastite breccias that make up igneous lithologic Units 2, 4, and 6. The aphyric basalt has rare olivine phenocrysts that form the center of radially arranged plagioclase microlites. The olivine crystals are typically subhedral (and sometimes euhedral) in shape and up to 1.6 mm in size. The groundmass is glassy and cryptocrystalline to microcrystalline with up to 1% vesicles smaller than 1.5 mm in some of the pieces. Clinopyroxene is rare and was only observed in the groundmass for Units 5 and 7 (based on thin sections TS116 through TS118; Figure **F21D**).

Igneous lithologic Units 2, 4, and 6 are recorded as hyaloclastite breccia with clasts of volcanic glass (up to 10 mm) in Units 2 and 4 and larger, angular aphyric basalt clasts (up to 7 cm) in Unit 6 (Figure **F19B**). The volcanic glass in both the glass shards and the

Figure F19. Basement basalt features, Hole U1434A, Unit IV. A. Aphyric basalt with alteration halos (light yellowish brown) along margins of subangular basalt pieces (14R-1A, 0–30 cm; Unit 5). B. Hyaloclastite breccia with larger blocky fragments of aphyric basalt (15R-1A, 56–86 cm; Unit 6).

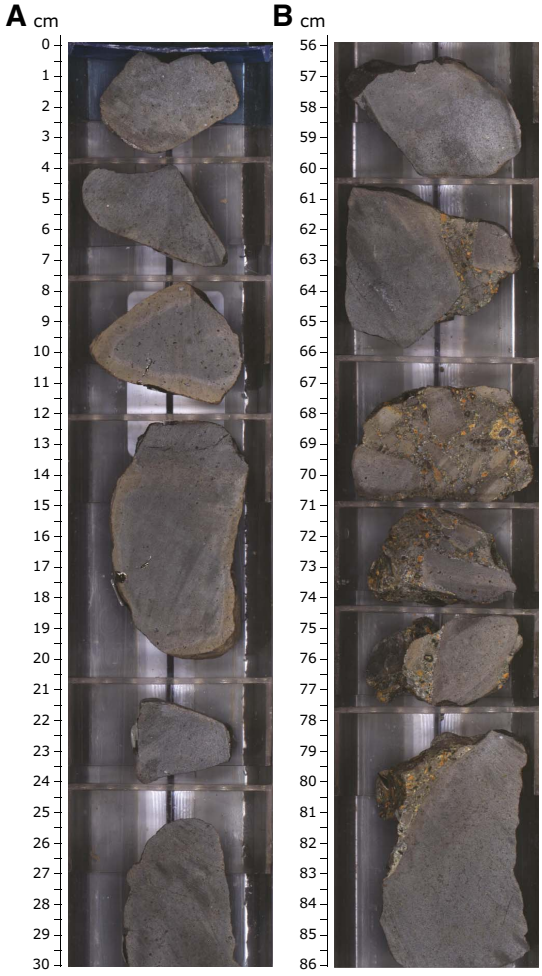

Figure F20. Interpillow hyaloclastite breccia, Hole U1434A, Unit IV. A, B. 11R-1, 17–23 cm (wet surface). C, D. 13R-1, 24–31 cm (wet surface; enhanced in Adobe Photoshop).

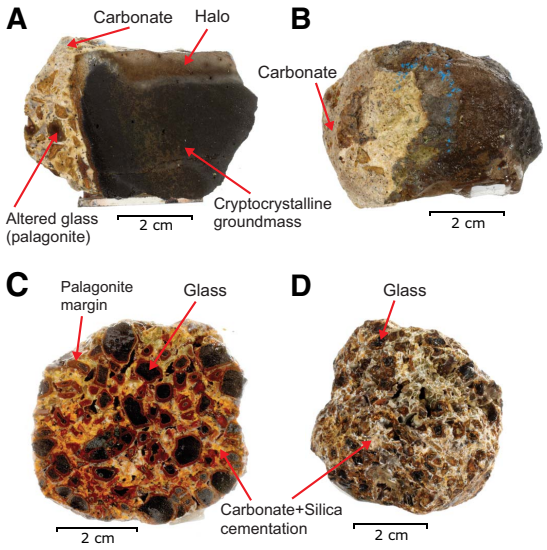

Figure F21. Hyaloclastite breccia, Hole U1434A, Unit IV (PPL). Pala = palagonite, Carb = carbonate. A, B. 11R-1, 17–19 cm; TS110. C, D, E. 13R-1, 13–18 cm; TS114.

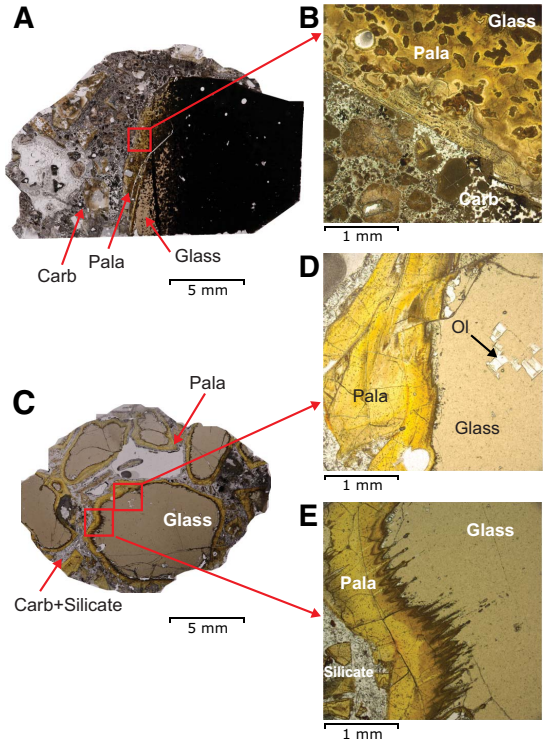

chilled margins of the larger aphyric basalt clasts is generally unaltered, except for a narrow rim that is replaced by palagonite (Figures **F20, F21**). Based on microscope observation, sparse well-preserved microphenocrysts of olivine (Figure **F21D**) as well as plagioclase are found in the volcanic glass, confirming the general phenocryst phase assemblage of olivine + plagioclase. Drilling at Site U1434 terminated at 308.65 mbsf, after encountering sustained hole instabilities.

Interpretation of the igneous succession at Site U1434

Site U1434 is located ~40 km away from Site U1433 and is closer to the fossil spreading axis of the Southwest Subbasin. This site is also close to a nearby seamount (Figures **F1, F3**). We recovered only 3.05 m of basalt after penetrating 30.38 m into igneous basement. Seven igneous lithologic units were recorded and include pillow basalt alternating with hyaloclastite breccia. Because no characteristic curved chilled margins, vesicle banding, or pillow basalt fractures were observed, this succession could be interpreted as the remnants of a thicker autobrecciated pillow lava flow. The phase assemblage consisting of olivine phenocrysts with plagioclase, and clinopyroxene in the groundmass, is typical of that of MORB and, in conjunction with geochemical evidence, we conclude that the basement basalt at Site U1434 is MORB (see **Geochemistry**).

Alteration

Similar to Site U1433, igneous basement basalt recovered at Site U1434 shows a low-temperature alteration assemblage that includes clay, Fe oxide, carbonate, and celadonite. Some fresh basaltic glass is preserved near the pillow basalt margins and in clasts making up the hyaloclasite breccia, but some are partly altered to palagonite,

Figure F22. Basalt, Hole U1434A, Unit IV. A. Aphanitic basalt with plagioclase (plg) microlites showing variolitic textures, leaving a large part of (devitrified) mesostasis (12R-1, 63–66 cm; TS113; PPL). B. Similar to A, but with a higher proportion of plagioclase microlites (14R-1, 4–8 cm; TS116; PPL). C. Small olivine (ol) microphenocrysts with euhedral crystal shape (11R-1, 44–46 cm; TS111; XPL). D. Patch with clinopyroxene (cpx) growing interstitially between plagioclase, whereas the rest of the mesostasis remains free of clinopyroxene (15R-1, 57–59 cm; TS117; PPL).

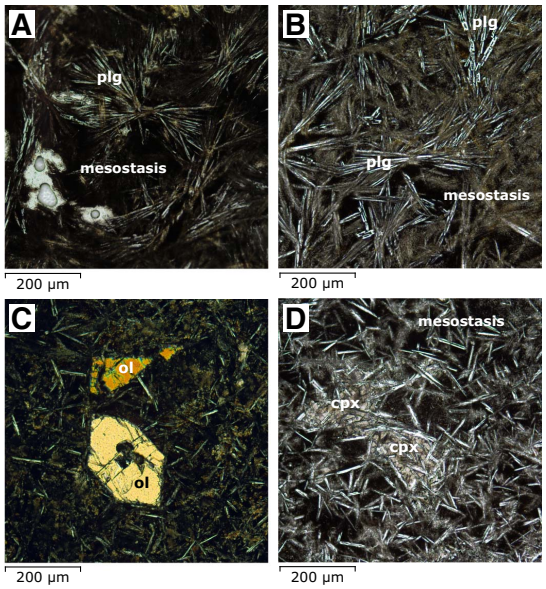

ranging in color from orange to brown. The few vesicles are not filled or are partly filled with Fe oxide, saponite/clay, celadonite, and carbonate. Alteration veins are uncommon, with only two thin carbonate-filled veins recorded. Based on macroscopic and thin section observations, the overall alteration style is characterized by the following categories:

- Patchy background alteration evenly distributed throughout the groundmass and mesostasis of the basalt;
- Alteration halos at the margins of basalt fragments;
- Partial palagonitization of glass fragments in hyaloclastite breccia; and
- Partial vesicle fillings (Figure **F23**) by secondary minerals, typically Fe oxide, clay, celadonite, and carbonate, in decreasing order.

Alteration phases

Alteration in the basement of Site U1434 is characterized by formation of celadonite, saponite/clay, carbonate, brown palagonite, and Fe oxide, consistent with interaction of basalt with oxidative seawater at low temperatures. Most of the crypto- to microcrystalline basalt fragments have patches with light brown to brown alteration colors in their groundmass. Mostly unaltered plagioclase microlites exist in the groundmass.

Alteration of primary minerals

Larger olivine microphenocrysts are partially altered to secondary minerals along cracks and margins but are mostly fresh in the volcanic glass. Plagioclase microlites in the groundmass are fresh or only slightly altered. Clinopyroxene is rare and microcrystalline in this basalt but appears relatively unaltered in thin section.

Figure F23. Vesicle fillings, Hole U1434A (PPL). A. Saponite (Sap) partially filling vesicle (11R-1, 44–46 cm; TS111). B. Saponite partially filling vesicle (14R-1, 4–8 cm; TS116). C. Fe oxide and saponite completely filling vesicle (15R-1, 57–59 cm; TS117). D. Saponite and carbonate (Carb) completely filling vesicle (15R-1, 79–81 cm; TS118).

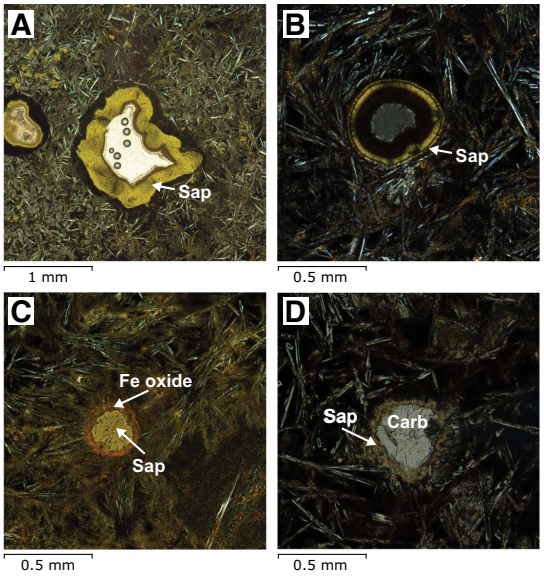

Background alteration and halos

Background alteration at Site U1434 accounts for the majority of the alteration and is pervasive throughout the units. No downhole trend of alteration extent can be observed. The background alteration is most evident in the crypto- to microcrystalline basalt pieces, with formation of secondary minerals such as Fe oxide, saponite/clay, celadonite, and carbonate, particularly in patches in the mesostasis. Alteration halos exist in the margin of many basalt pieces, with colors ranging from yellowish brown to brown (Figure **F19A**).

Vesicles

Vesicles make up <1% of the recovered basement basalt in Hole U1434A. Based on thin section observations, vesicles are only partly filled with Fe oxide, palagonite, celadonite, and carbonate (Figure **F23**).

Hyaloclastite breccia

Igneous lithologic Units 2, 4, and 6 are composed of cryptocrystalline to microcrystalline pillow basalt pieces and glass as clasts that are cemented by carbonate, clay minerals, and likely also some silica. This basaltic glass is mostly well preserved with minor alteration to greenish palagonite, usually along rims (Figures **F19B, F20, F21**).

Interpretation of alteration

Alteration of basalts recovered at Site U1434 occurred under oxidative conditions with seawater/fluids, as shown by the secondary mineral assemblages of carbonate, Fe oxide, celadonite, and brown palagonite, which is a typical alteration style for MORBs and is recognized at previous sites, such as Integrated Ocean Drilling Program Site U1367 (Expedition 329 Scientists, 2011). Most vesicles are not filled or are partly filled with Fe oxide, saponite, celadonite, and carbonate, indicating limited fluid flow and alteration extent at this site. Uncommon occurrence of alteration veins is consistent with the limited fracturing in those basalt pieces.

Structural geology

Site U1434 lies on the southern shoulder of the relict spreading ridge of the Southwest Subbasin, South China Sea (Figure F1). A northwest–southeast oriented seismic profile across this site shows a local depression with one volcanic seamount located immediately to the north (Figure F3). Seismic reflections above the basement are generally continuous without obvious evidence of faults or unconformities, although the reflectors are slightly curved on the upper part.

The core recovery in Hole U1434A is relatively poor. We observed traces of deformation in consolidated sediment and basement rock and measured the dip orientation and angle of fractures and veins. Compared with Holes U1431E and U1433B, fractures and veins at this site are rare. However, it is unclear if this is because of poor recovery or if the basement has fewer fractures and veins at this site. Only 2 fractures and 4 veins were measured. Most of the fractures observed in the sedimentary rocks are drilling induced, except one with a slight offset in the claystone (Figure F24). The hanging and foot walls are now fused, with no gap along the fracture plane. We interpret that this fracture might have been formed before consolidation of the clay. As a result of the very poor recovery of the basement, most of the basalts are broken pieces with lengths between 3 and 8 cm. Only 4 veins are identified in separate basalt pieces. These veins are straight with no more than 0.2 cm thickness (Figure F25) and are filled with white carbonate and brown Fe oxide.

Figure F24. A closed fault observed in the claystone, Interval 349-U1434A-10R-1A, 65-74 cm. (A) Line-scan image; (B) Geological interpretation. White line traces the fault with arrow indicating direction of offset. White brush strokes are drawn tracing the claystone laminations, whose orientation change slightly between hanging and foot walls.

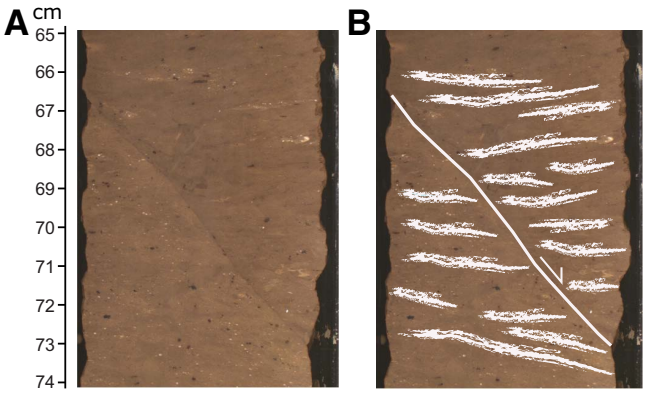

Figure F25. Typical fracture and veins observed in the basalt, Interval 349-U1434A-11R-1A, 91–96 cm. Veins are linear with small thickness, infilled with Fe-oxide. The fracture is drilling induced along an existing vein.

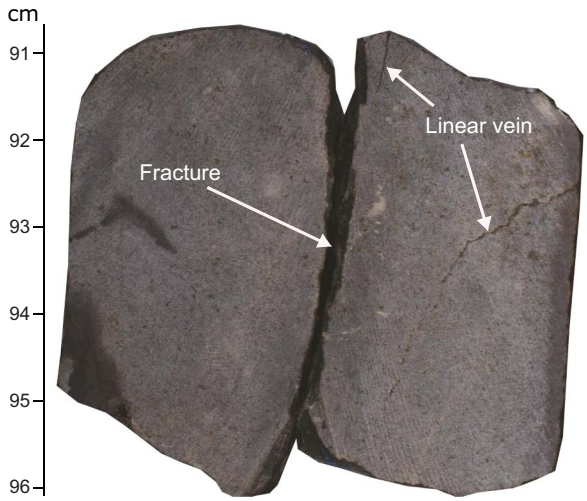

Geochemistry

Interstitial water chemistry

We collected 5 whole-round samples (10–15 cm long) for interstitial water measurements from 207.9–275.0 mbsf in Hole U1434A at a frequency of one sample per core. No interstitial water samples were taken when core recovery was <10%. Interstitial water chemistry data are given in Table T7 and shown in Figures F26 and F27.

Chloride, bromide, and sodium

Downhole profiles of chloride, bromide, and sodium in Hole U1434A are shown in Figure F26. Chloride, bromide, and sodium concentrations vary with depth, with values close to modern seawater in lithostratigraphic Unit I, reaching minima in the greenish nannofossil-rich claystone of Unit II, and increasing to near modern seawater values in the yellowish brown claystone of Unit III.

Alkalinity, sulfate, calcium, and magnesium

Alkalinity, sulfate, calcium, and magnesium profiles are shown in Figure F27. Alkalinity increases from 0.5 mM at ~210 mbsf to a maximum 3.5 mM at the boundary between lithostratigraphic Units II and III, before decreasing to 2.4 mM at 275 mbsf in Unit III. Sulfate concentrations decrease from 27.2 mM in Unit I to 26.5 mM in Unit II and then increase to ~27.6 mM in Unit III. Calcium concentrations are much higher than the modern seawater value (10.5 mM) throughout the cored section, decreasing from 26.5 mM to 17.9 mM at the bottom of the hole. Magnesium concentrations are much lower than the modern seawater value (54 mM), increasing from 33 to 44 mM downhole, probably due to clay ion exchange.

Headspace gas geochemistry

Headspace gas was monitored in cores from Hole U1434A as part of the shipboard safety and pollution prevention program. Methane concentrations in all samples from Hole U1434A are very low (<5 ppmv). Ethane and propane were not detected (Figure F28; Table T8).

Bulk carbon and nitrogen analysis

Total organic carbon (TOC), $CaCO_3$, total nitrogen, and TOC to nitrogen (C/N) ratio distributions for Hole U1434A are listed in Table T9 and illustrated in Figure F29. Because of the low core recovery, only six samples were collected for carbon and nitrogen content analysis. The $CaCO_3$ content is <10 wt% in the four samples taken above 260 mbsf, but is higher (15–30 wt%) in the two samples from the lower part of lithostratigraphic Unit III. TOC is low (<0.5 wt%) throughout the hole. Total nitrogen is low, except for one higher value (1.53 wt%) from a sample near the top of Unit II. The C/N ratio is also generally low (<5), which indicates a dominant marine

Table T7. Interstitial water major element concentrations, salinity, pH, alkalinity, sulfate, chloride, bromide, calcium, magnesium, sodium, and potassium Hole U1434A. **Download table in .csv format.**

Figure F26. Interstitial water bromide, chloride, and sodium, Hole U1434A.

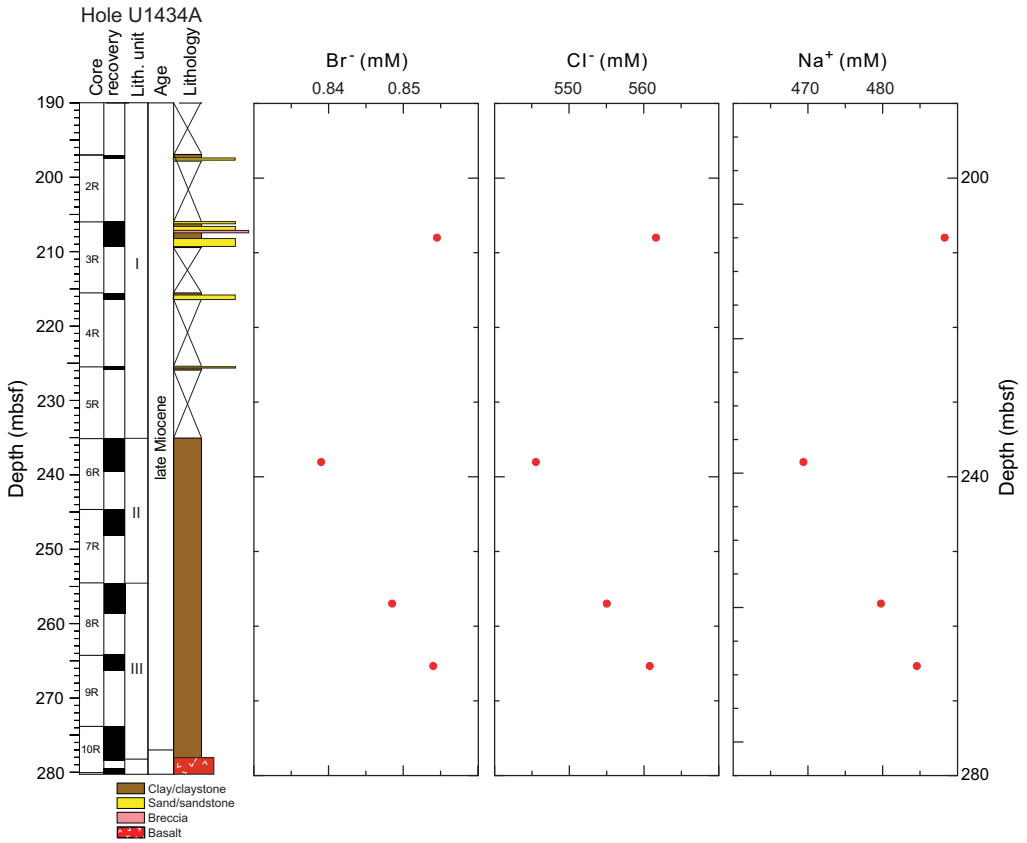

Figure F27. Interstitial water alkalinity, sulfate, calcium, and magnesium, Hole U1434A.

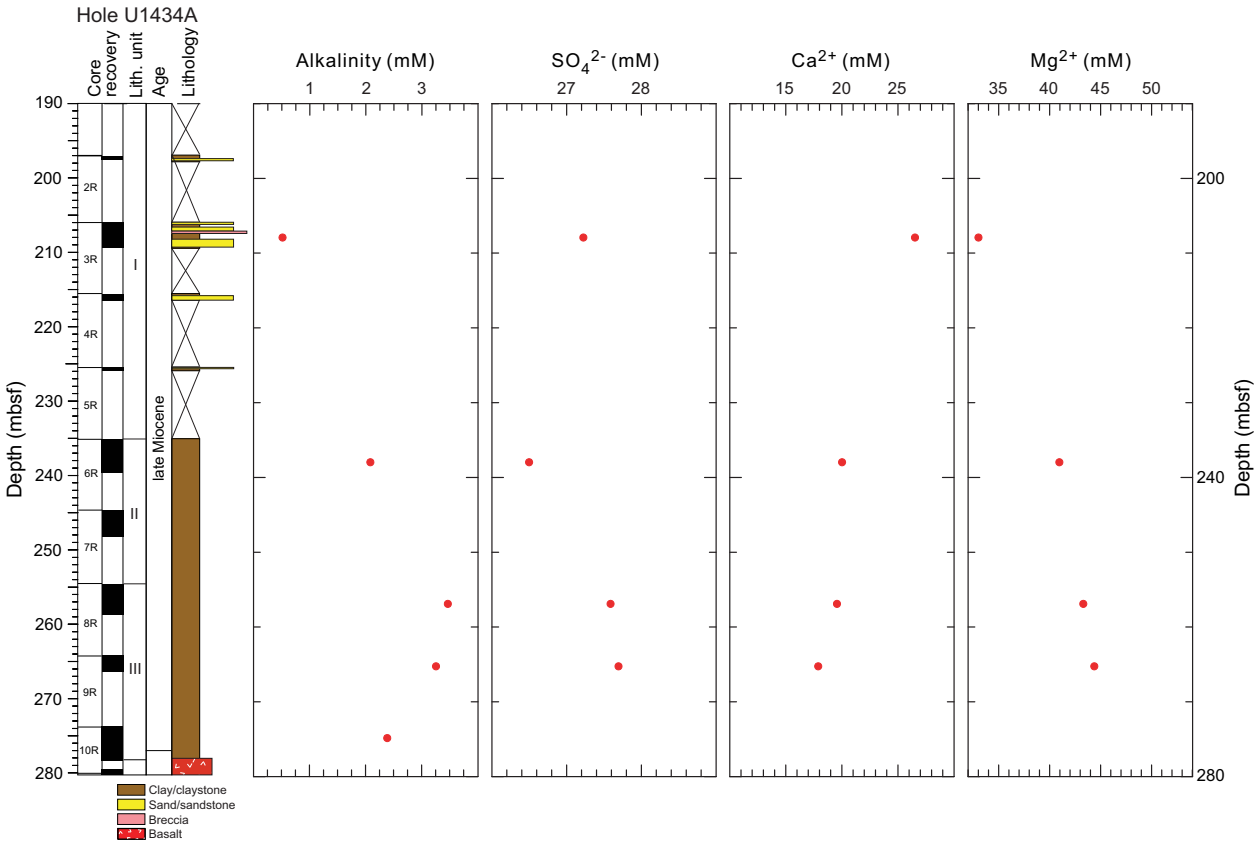

Figure F28. Methane in headspace gas, Hole U1434A.

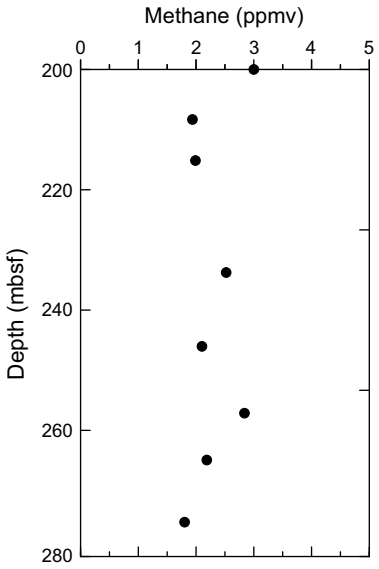

Table T8. Headspace sample hydrocarbon concentrations, methane, Hole U1434A. **Download table in .csv format.**

Table T9. Carbon and nitrogen contents, $CaC0_3$, TOC, TC and C/N ratios, Hole U1434A. **Download table in .csv format.**

source for the organic matter. One sample in Unit III has a higher C/N ratio (~23), which could indicate an influx of terrestrial organic matter.

Igneous rock geochemistry

Six igneous rock samples from Cores 349-U1434A-10R through 15R were analyzed for concentrations of major and trace elements by inductively coupled plasma–atomic emission spectroscopy (Figure **F30;** Table **T10**).

Loss on ignition values, which serve as a rough indicator of the overall level of alteration in the rocks, are generally low, ranging from 1.05 to 1.93 wt%. One sample has a total weight percentage for the major element oxides of 120.9 wt%, and the other five samples vary from 101.8 to 105.4 wt%. The monitored standards BCR-2 and HBVO-2 measurements were consistent and within recommended values; the high total weight percentage for these samples is most likely due to large weighing errors resulting from ship motion during the transit from Site U1434 to U1435. For comparison with data from other sites, measured major element total values were normalized to 100 wt%. The samples have moderate K_2O (0.11–0.29 wt%), TiO_2 (1.51–1.69 wt%), MgO (5.50–7.22 wt%), Fe_2O_3 (9.89–11.54 wt%), and Na_2O (2.77–3.65 wt%) and high SiO_2 (50.6–55.5 wt%), Al_2O_3 (13.83–15.27 wt%), and CaO (9.46–11.00 wt%) concentrations, compared with average basalt. Concentrations of major elements vary within narrow ranges for all measured samples.

When plotted on the alkali versus silica diagram of volcanic rock types (Le Maitre et al., 1989) (Figure **F31**), five samples are tholeiitic

Figure F29. Calcium carbonate, TOC, total nitrogen (TN), and C/N ratio, Hole U1434A.

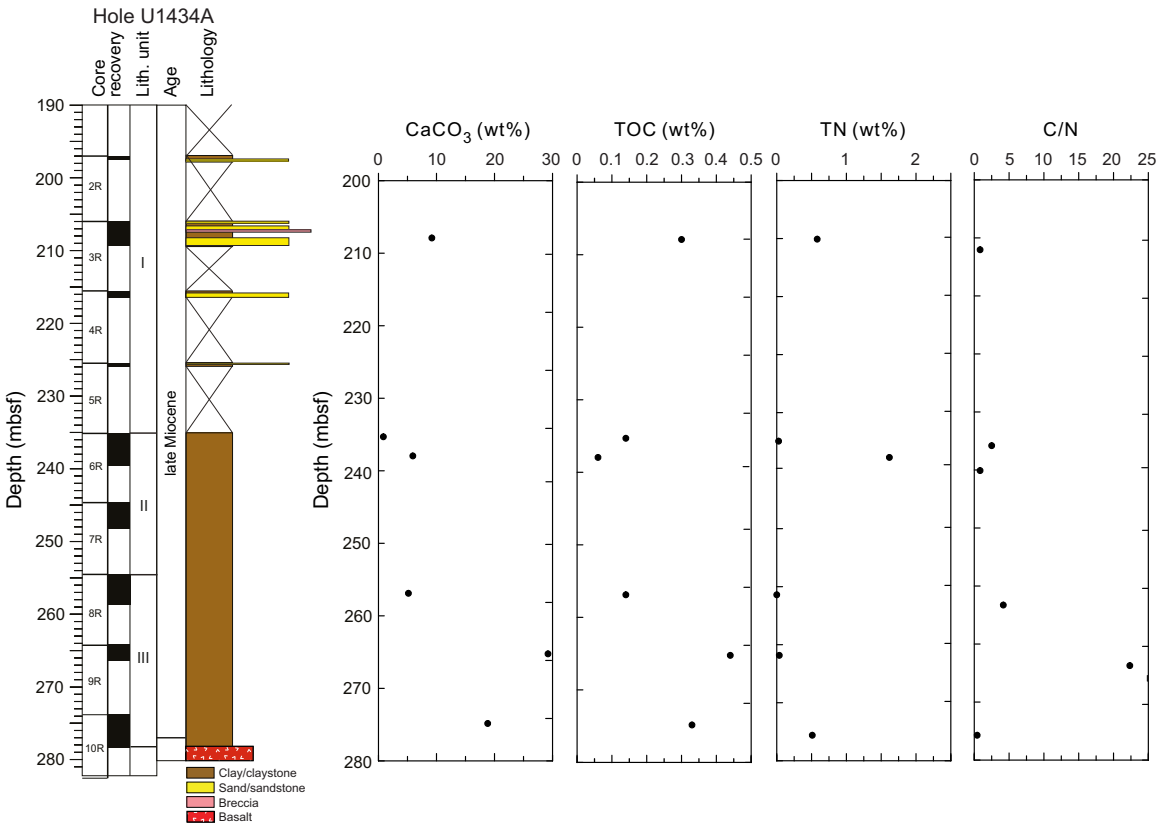

Figure F30. Loss on ignition (LOI) and major element composition of igneous rock samples, Hole U1434A. Lithostratigraphy column includes lithology, igneous lithologic units (1–7), and lithostratigraphic units (III and IV). EOH = end of hole.

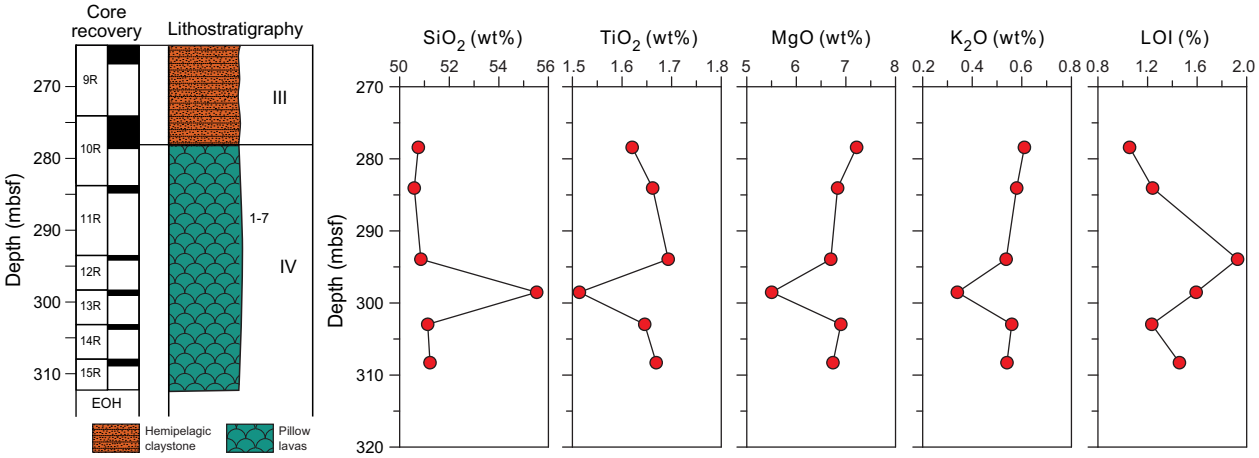

Table T10. Major and minor element compositions of igneous samples, SiO_2, TiO_2, Al_2O_3, $Fe_2O_3^T$, MnO, MgO, CaO, Na_2O, K_2O, P_2O_5, LOI, Ba, Co, Cr, Sc, Sr, V, and Zn, Hole U1434A. **Download table in .csv format.**

Figure F31. Total alkalis vs. silica, Hole U1434A. Classification of volcanic rock types from Le Maitre et al. (1989). The dashed blue line divides data between tholeiitic and alkalic lavas of Hawaii (Macdonald and Katsura, 1964; Macdonald, 1968). Shown for comparison are data for Indian Ocean MORB from the Geochemical Rock Database (**georoc.mpch-mainz.gwdg.de**), seamounts in the SCS (Tu et al., 1992; Hékinian et al., 1989), OIB in the Hainan Island (Wang et al., 2012), and Pacific Ocean MORB (Zhang et al., 2009, 2012a, 2012b, 2013).

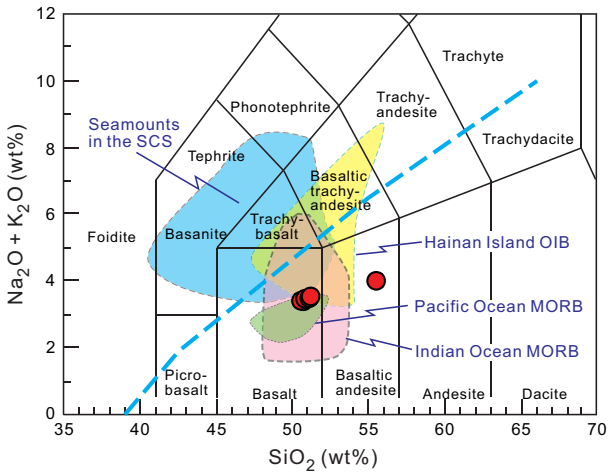

basalt and one plots in the basaltic andesite field. As shown in Figure **F32,** these rocks are similar to Pacific and Indian Ocean MORB and are distinct from the Hainan Island ocean-island basalt (OIB) and the basalt from seamounts in the South China Sea. Thus, the basalt samples from Cores 349-U14344A-10R through 15R are tholeiitic basalt, representative of South China Sea MORB.

Figure F32. TiO_2 vs. P_2O_5, V, and Sr, Hole U1434A. Shown for comparison are data for Indian Ocean MORB from the Geochemical Rock Database (**georoc.mpch-mainz.gwdg.de**), seamounts in the SCS (Tu et al., 1992; Hékinian et al., 1989), OIB in the Hainan Island (Wang et al., 2012), and Pacific Ocean MORB (Zhang et al., 2009, 2012a, 2012b, 2013).

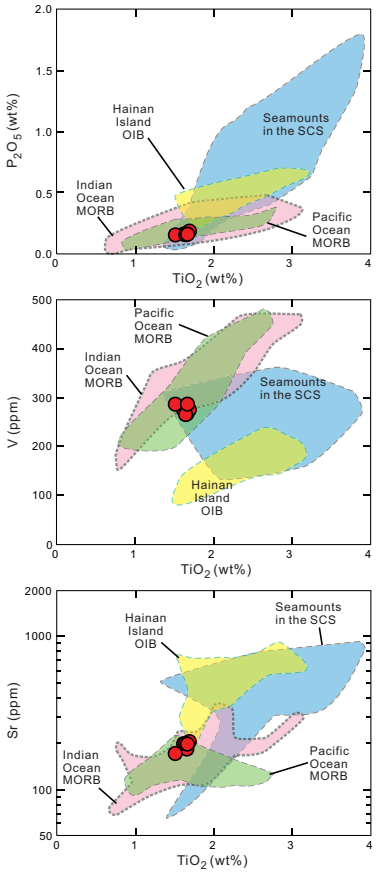

Microbiology

Our goal for microbiological research at Site U1434 was to collect and preserve samples for shore-based characterization of microbial communities. We collected samples on a routine basis throughout the cored intervals and on a case-by-case basis according to features in the cores that suggested the presence of important geological interfaces. In addition, we collected samples for measuring contamination, using microspheres and fluid community tracers.

Specific depths sampled for microbiology at Site U1434 are shown in Figure **F33.** Coring in Hole U1434A yielded 6 routine, 5–10 cm whole-round samples to be used for microbiological analysis from 208 to 275 mbsf. We collected whole-round samples for microbiology adjacent to samples for interstitial water measurements in order to understand proximal interstitial water chemistry (see **Geochemistry**).

We collected and preserved 13 samples either from the split cores on the sampling table or from basement samples shortly after the samples were retrieved from the catwalk for investigating the microbiology of interfaces using lipid and nucleic acid analyses. We obtained these samples between 207 and 303 mbsf in Hole U1434A. We selected these samples by depending on recognition of key intervals and through consultation with sedimentologists or petrologists.

Microbiological analyses

Most of the samples collected at Site U1434 were preserved for shore-based analysis. Samples to be used for DNA and RNA extractions and sequencing were frozen at –80°C, and samples to be used for lipid extraction and analysis were frozen at –80° or –20°C. Portions of the whole-round samples were selected for cultivation-based studies to enrich for anaerobic heterotrophs and autotrophs.

Contamination testing

We used two different methods of contamination testing during coring at Site U1434. Microsphere tracers were used with the RCB coring system in Hole U1434A by adding them to the core catcher sub in Cores 349-U1434A-3R through 14R (208–303 mbsf; Figure **F33**). Two microsphere samples were collected from each of those cores: one from scrapings of the core surface and one as a subsample from the interior of each sample. Microscopic counts of the microspheres in these samples will be performed in shore-based laboratories using the Procedure for Curation of DeepBIOS (**www.kochi-core.jp/DeepBIOS**).

Six fluid community tracer (FCT) samples were collected either from the drilling fluids that drained from the core liners when cores arrived on the catwalk or from a sampling port near the mud pumps on the drill rig floor during active coring. The fluids collected for FCT samples correspond to cores obtained between 208 and 293 mbsf (Figure **F33**). Microbial community DNA and lipids from FCT samples will be compared to the same measurements made on the microbiology samples to determine if the drilling fluids contain microbes that can be regularly tracked as recognizable contaminant taxa.

Figure F33. Collection depths of microbiology whole-round and interface samples and contamination testing samples, Hole U1434A. Number "2" means two samples were collected at the specified depth.

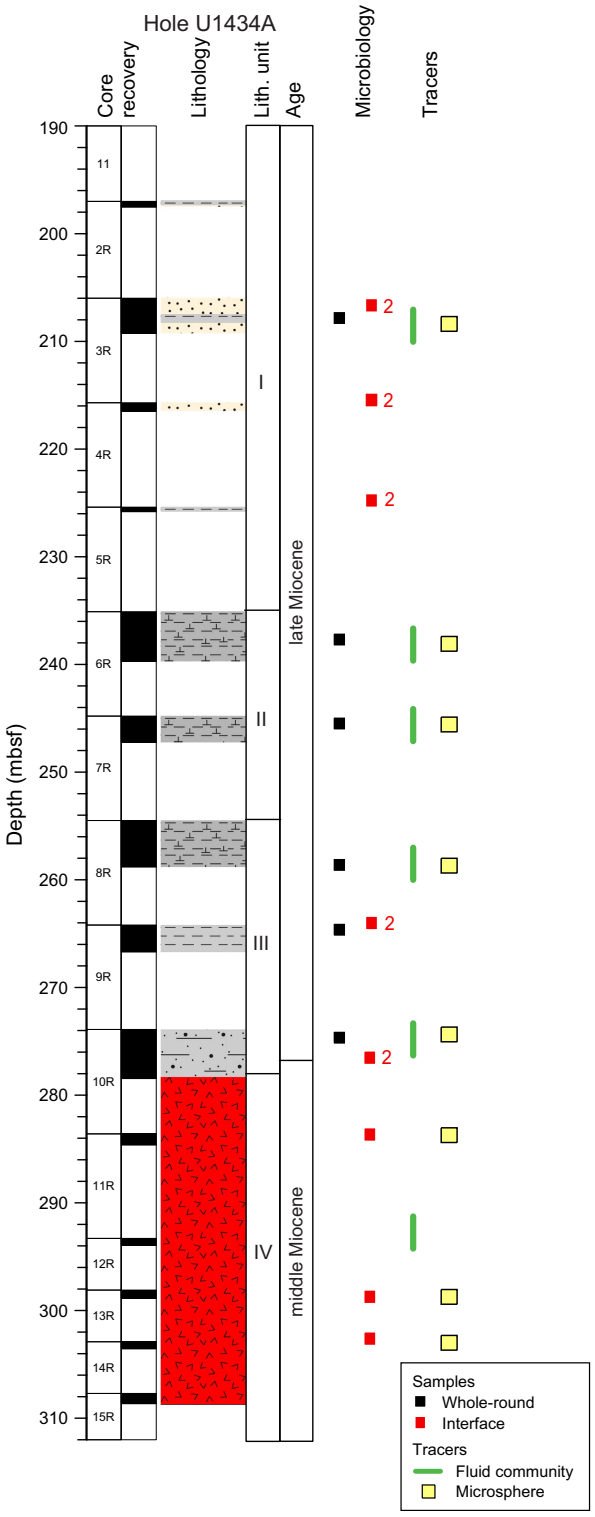

Paleomagnetism

At Site U1434, the pass-through magnetometer measurements on all archive-half cores were conducted using the 2G superconducting rock magnetometer, with demagnetization steps of 0, 5, 10, and 20 mT. The results were analyzed using Zijderveld diagrams (Zijderveld, 1967), and the characteristic remanent magnetization direction was obtained using principal component analysis (Kirschvink, 1980).

Natural remanent magnetization of sedimentary cores

Downhole variation in paleomagnetic data obtained from Hole U1434A is illustrated in Figure **F34.** The generally low recovery rate limits magnetic characterization of sediment and basement rock at this site. Natural remanent magnetization (NRM) intensity ranges between 0.001 and 0.1 A/m for sediment units and increases to several amperes per meter (A/m) for basalt units (Figure **F34**), suggesting that the basalt units contain more iron oxide than the overlying sediment. Most cores exhibit positive inclinations, with the maximum values close to ~90°. Similar to all previous sites, after 20 mT alternating field (AF) demagnetization, the near-vertical inclinations caused by drilling-induced remagnetization shift to lower values for sediment; NRM intensity of sediment significantly decreases but only slightly for basalt. This indicates that basalt contains more high-coercivity minerals, mostly in single domain state. In contrast, sediment contains more pseudo-single domain or multiple domain magnetic particles.

Figure F34. Paleomagnetic measurements of NRM inclination and intensity on archive core sections of sediment after 0 mT (red) and 20 mT (blue) AF demagnetization for Hole U1434A.

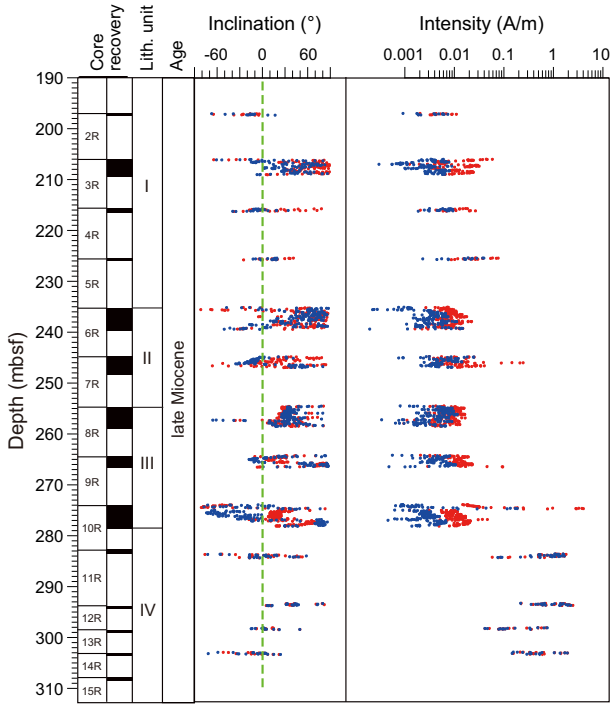

Paleomagnetic demagnetization results and magnetostratigraphy

Representative vector plots (Zijderveld, 1967) showing magnetic behavior of detailed AF demagnetization are given in Figure **F35.** Generally, behavior can be classified into two groups. The first group (sediment) exhibits relatively larger vertical overprints (Figures **F35A, F35B**), which can be removed by 10 mT AF demagnetization. In contrast, the second group (basalt) is more resistant to AF demagnetization (Figure **F35C, F35D**).

Because of the poor recovery in Hole U1434A, only fragmentary patterns of magnetic polarity can be observed, rendering it difficult to construct a reliable magnetostratigraphy for the hole (Figure **F36**). Nevertheless, available calcareous nannofossil ages allow us to tentatively correlate certain parts of the magnetic polarity interval recorded in the sediment with the geomagnetic polarity timescale (GPTS; Gradstein et al., 2012). Biostratigraphic samples at ~278 mbsf have been assigned an age <11.9 Ma (see **Biostratigraphy**); therefore, we interpret that sediment with observed negative inclinations at this depth were likely deposited within Chron C5r (11.056–12.049 Ma). The dominant long positive inclinations between ~250 and 270 mbsf may represent the Subchron C5n (9.984–11.06 Ma). The short positive polarity zone between ~235 and 240 mbsf appears to have recorded Chron C4An (8.771–9.015 Ma), and the positive polarity zone between 205 and 210 mbsf can be tentatively assigned to Chron C4n at ~7.15 Ma. Such a pattern also indicates a low sedimentation rate for sediment recovered at this site.

Figure F35. Representative vector end-point diagrams (Zijderveld, 1967) of magnetization directions for (A, B) sediment and (C, D) basalt samples through stepwise alternating field demagnetization.

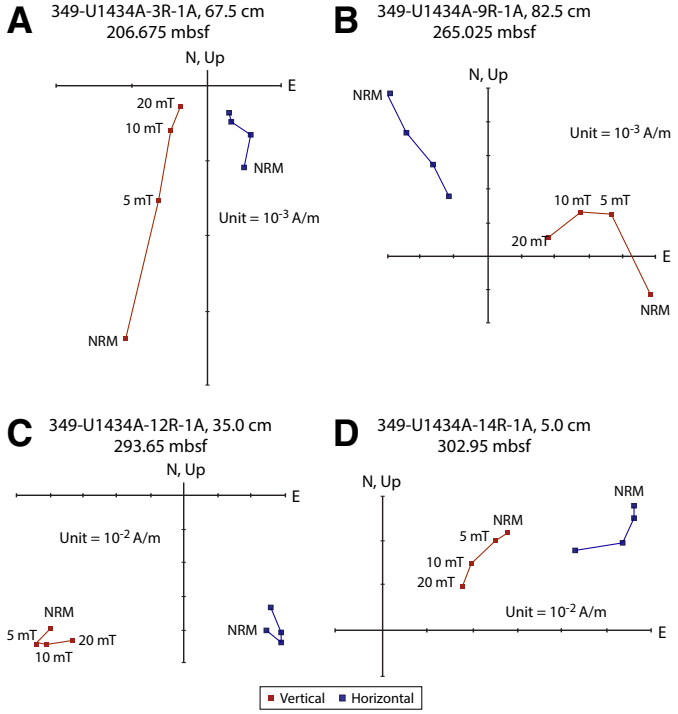

Figure F36. Magnetostratigraphic results with biostratigraphic age correlation for Hole U1434A using paleomagnetic inclination after 20 mT alternating field demagnetization. For GPTS (Gradstein et al., 2012), black = normal polarity and white = reversed polarity.

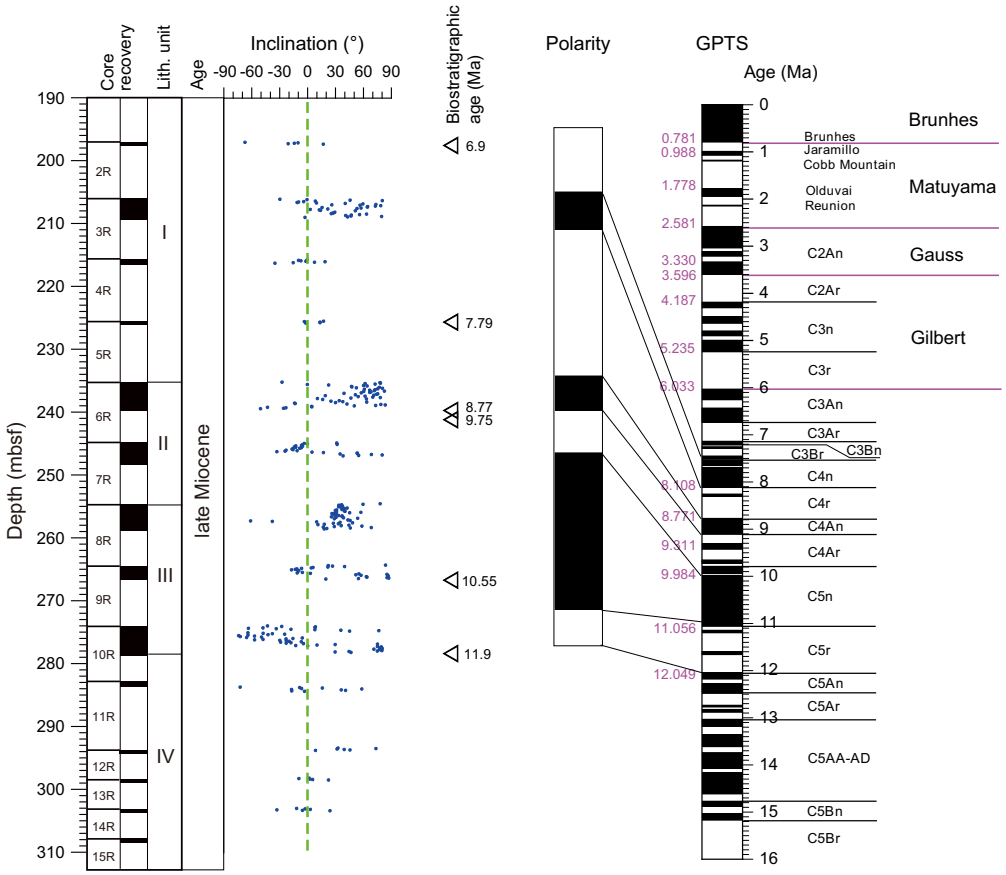

The basalt unit below 280 mbsf appears to have recorded positive polarity. This coincides with Sites U1431 and U1433, at which positive polarities are observed for the upper part of the basalt units. These preliminary magnetostratigraphic signatures at Site U1434 await verification by shore-based studies.

Physical properties

At Site U1434, we measured physical properties on whole-round cores (bulk density from gamma ray attenuation [GRA], magnetic susceptibility, and natural gamma radiation [NGR]), on split cores (thermal conductivity and *x*-caliper *P*-wave velocity), and on discrete samples (porosity, moisture, and density) (Figure **F37**). Because of the low recovery rate, measurements of physical properties show significant gaps between measured intervals. No discrete samples were taken for physical property measurements in the basalt sections because of poor recovery (lithostratigraphic Unit IV; 278.27–312.50 mbsf).

Physical property measurements

After whole-round core measurements were made, data points out of range were removed. The whole-round core data were then smoothed using a 10-point average moving window (Figure **F37**). Magnetic susceptibility values in Hole U1434A are relatively uniform (30×10^{-5} to 70×10^{-5} SI; average = 50×10^{-5} SI) in lithostratigraphic Unit I (197.00–235.10 mbsf), which consists of interbedded claystone and volcaniclastic sandstone. In Unit II (nannofossil claystone; 215.10–254.59 mbsf), magnetic susceptibility increases slightly to a range of 30×10^{-5} to 80×10^{-5} SI, with an average of 60×10^{-5} SI. In Unit III (yellowish brown claystone; 254.59–278.27 mbsf), magnetic susceptibility reaches a minimum (20×10^{-5} SI) at the Unit II/III boundary and then increases to a range of 60×10^{-5} to 90×10^{-5} SI at the Unit III/IV boundary. The range of magnetic susceptibility values in the basalt section (Unit IV; 278.27–308.65 mbsf) is 10×10^{-5} to 90×10^{-5} SI.

Because of the low recovery rate, NGR data are only available for 205–212 mbsf in Unit I, with values ranging from 20 to 30 counts/s. NGR decreases from ~45 to ~30 counts/s in Unit II, stays relatively uniform at ~25 counts/s in Unit III, and then drops to low values <5 counts/s in the basalt of Unit IV. *P*-wave velocity ranges from 1950 to 3100 m/s in Unit I, drops to ~1850 m/s in the claystone of Units II and III, and was not measured on the basalt pieces of Unit IV. Bulk density remains relatively constant (~1.8 g/cm^3) in Unit II and the top half of Unit III and then increases slightly to 1.8–2.0 g/cm^3 in the sediment layer (275–278 mbsf) immediately above the basaltic section. Dry bulk density remains constant (1.2 g/cm^3) in Unit I, decreases gradually through Unit II and top half of Unit III, reaches a minimum (~0.7 g/cm^3) at 265 mbsf, and then increases to 1.3 g/cm^3 in the sediment layer (275–278 mbsf) immediately above the basalt. Grain density is quite variable through Units I and II and reaches 3.25 g/cm^3 in the yellowish brown clays of Unit III. Porosity increases with depth from ~50% to ~75% in Units I and II and the top half of Unit III and then drops to 50% in the sediment layer immediately above the basalt.

Figure F37. Physical property measurements, Hole U1434A. Dashed line marks the lithostratigraphic boundary between Units II and III. WRMSL = Whole Round Multisensor Logger, SHMSL = Section-Half Multisensor Logger.

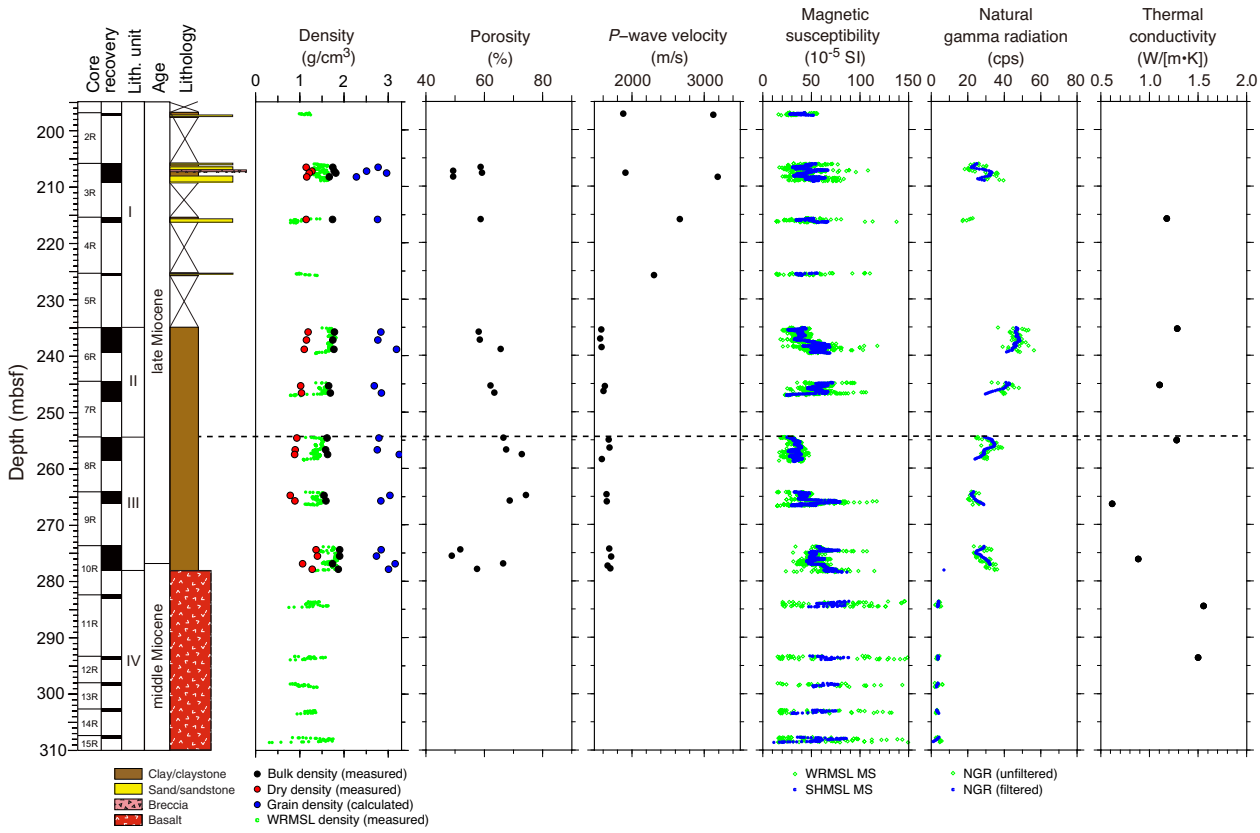

Thermal conductivity remains constant (~1.1–1.3 W/[m·K]) in Units I and II, drops to 0.7–0.9 W/(m·K) in Unit III, and then increases to ~1.5 W/(m·K) in Unit IV.

Data interpretation and lithology correlation

In general, physical properties correlate with lithology, composition, and lithification. In Hole U1434A, the observed range of values for magnetic susceptibility (30×10^{-5} to 80×10^{-5} SI) and NGR (25–45 counts/s) in lithostratigraphic Units I–III are typical for clay material, which dominates the sediment layers. The low NGR values in Unit IV correspond to the basalt layer. Magnetic susceptibility values in the basalt range from 10×10^{-5} to 90×10^{-5} SI, which is much lower than typical basalt. This is probably at least partly due to the poor recovery and the relatively low volume of basalt pieces in the core liner.

High grain densities in the claystone of Units II and III suggest the presence of heavy minerals, such as hematite. Porosity measured on discrete samples increases from 40% to 60% with depth, which might be correlated to lithification and composition of the claystone.

References

Briais, A., Patriat, P., and Tapponnier, P., 1993. Updated interpretation of magnetic anomalies and seafloor spreading stages in the South China Sea: implications for the Tertiary tectonics of Southeast Asia. *Journal of Geophysical Research: Solid Earth,* 98(B4):6299–6328. **http://dx.doi.org/10.1029/92JB02280**

Bryant, W.R., and Bennett, R.H., 1988. Origin, physical, and mineralogical nature of red clays: the Pacific Ocean Basin as a model. *Geo-Marine Letters,* 8(4):189–249. **http://dx.doi.org/10.1007/BF02281640**

Expedition 329 Scientists, 2011. Site U1367. In D'Hondt, S., Inagaki, F., Alvarez Zarikian, C.A., and the Expedition 329 Scientists, *Proc. IODP,* 329: Tokyo (Integrated Ocean Drilling Program Management International, Inc.). doi:10.2204/iodp.proc.329.105.2011.

Gradstein, F.M., Ogg, J.G., Schmitz, M.D., and Ogg, G.M. (Eds.)., 2012. *The Geological Time Scale 2012:* Oxford, UK (Elsevier).

Hékinian, R., Bonté, P., Pautot, G., Jacques, D., Labeyrie, L.D., Mikkelsen, N., and Reyss, J.-L., 1989. Volcanics from the South China Sea ridge system. *Oceanologica Acta,* 12(2):101–115.

Ishihara, T., and Kisimoto, K., 1996. Magnetic anomaly map of East Asia, 1:4,000,000 (CD-ROM version). Geological Survey of Japan, Coordinating Committee for Coastal and Offshore Geoscience Programs in East and Southeast Asia (CCOP).

Kirschvink, J.L., 1980. The least-squares line and plane and the analysis of palaeomagnetic data. *Geophysical Journal of the Royal Astronomical Society,* 62(3):699–718. **http://dx.doi.org/10.1111/j.1365-246X.1980.tb02601.x**

Le Maitre, R.W., Bateman, P., Dudek, A., Keller, J., Lameyre, J., Le Bas, M.J., Sabine, P.A., Schmid, R., Sorensen, H., Streckeisen, A., Woolley, A.R., and Zanettin, B., 1989. *A Classification of Igneous Rocks and Glossary of Terms:* Oxford, UK (Blackwell Science Publishing).

Li, C.-F., Lin, J., Kulhanek, D.K., Williams, T., Bao, R., Briais, A., Brown, E.A., Chen, Y., Clift, P.D., Colwell, F.S., Dadd, K.A., Ding, W., Almeida, I.H., Huang, X.-L., Hyun, S., Jiang, T., Koppers, A.A.P., Li, Q., Liu, C., Liu, Q., Liu, Z., Nagai, R.H., Peleo-Alampay, A., Su, X., Sun, Z., Tejada, M.L.G., Trinh, H.S., Yeh, Y.-C., Zhang, C., Zhang, F., Zhang, G.-L., and Zhao, X., 2015a. Expedition 349 summary. *In* Li, C.-F., Lin, J., Kulhanek, D.K., and the Expedition 349 Scientists, *Proceedings of the Integrated Ocean Drilling*

Program, 349: South China Sea Tectonics: College Station, TX (International Ocean Discovery Program). **http://dx.doi.org/10.14379/iodp.proc.349.101.2015**

Li, C.-F., Lin, J., Kulhanek, D.K., Williams, T., Bao, R., Briais, A., Brown, E.A., Chen, Y., Clift, P.D., Colwell, F.S., Dadd, K.A., Ding, W., Almeida, I.H., Huang, X.-L., Hyun, S., Jiang, T., Koppers, A.A.P., Li, Q., Liu, C., Liu, Q., Liu, Z., Nagai, R.H., Peleo-Alampay, A., Su, X., Sun, Z., Tejada, M.L.G., Trinh, H.S., Yeh, Y.-C., Zhang, C., Zhang, F., Zhang, G.-L., and Zhao, X., 2015b. Methods. *In* Li, C.-F., Lin, J., Kulhanek, D.K., and the Expedition 349 Scientists, *Proceedings of the Integrated Ocean Drilling Program, 349: South China Sea Tectonics:* College Station, TX (International Ocean Discovery Program). **http://dx.doi.org/10.14379/iodp.proc.349.102.2015**

Li, C.-F., Lin, J., Kulhanek, D.K., Williams, T., Bao, R., Briais, A., Brown, E.A., Chen, Y., Clift, P.D., Colwell, F.S., Dadd, K.A., Ding, W., Almeida, I.H., Huang, X.-L., Hyun, S., Jiang, T., Koppers, A.A.P., Li, Q., Liu, C., Liu, Q., Liu, Z., Nagai, R.H., Peleo-Alampay, A., Su, X., Sun, Z., Tejada, M.L.G., Trinh, H.S., Yeh, Y.-C., Zhang, C., Zhang, F., Zhang, G.-L., and Zhao, X., 2015c. Site U1433. *In* Li, C.-F., Lin, J., Kulhanek, D.K., and the Expedition 349 Scientists, *Proceedings of the Integrated Ocean Drilling Program, 349: South China Sea Tectonics:* College Station, TX (International Ocean Discovery Program). **http://dx.doi.org/10.14379/iodp.proc.349.105.2015**

Li, C.-F., Zhou, Z., Li, J., Chen, B., and Geng, J., 2008. Magnetic zoning and seismic structure of the South China Sea ocean basin. *Marine Geophysical Researches,* 29(4):223–238. **http://dx.doi.org/10.1007/s11001-008-9059-4**

Macdonald, G.A., 1968. Composition and origin of Hawaiian lavas. *In* Coats, R.R., Hay, R.L., and Anderson, C.A. (Eds.), *Studies in Volcanology—A Memoir in Honor of Howel Williams.* Memoir - Geological Society of America, 116:477–522. **http://dx.doi.org/10.1130/MEM116-p477**

Macdonald, G.A., and Katsura, T., 1964. Chemical composition of Hawaiian lavas. *Journal of Petrology,* 5(1):82–133. **http://petrology.oxfordjournals.org/content/5/1/82.abstract**

Pautot, G., Rangin, C., Briais, A., Tapponnier, P., Beuzart, P., Lericolais, G., Mathieu, X., Wu, J., Han, S., Li, H., Lu, Y., and Zhao, J., 1986. Spreading direction in the central South China Sea. *Nature,* 321(6066):150–154. **http://dx.doi.org/10.1038/321150a0**

Tu, K., Flower, M.F.J., Carlson, R.W., Xie, G., Chen, C.-Y., and Zhang, M., 1992. Magmatism in the South China Basin: 1. Isotopic and trace-element evidence for an endogenous Dupal mantle component. *Chemical Geology,* 97(1–2):47–63. **http://dx.doi.org/10.1016/0009-2541(92)90135-R**

Wang, X.-C., Li, Z.-X., Li, X.-H., Li, J., Liu, Y., Long, W.-G., Zhou, J.-B., and Wang, F., 2012. Temperature, pressure, and composition of the mantle source region of late Cenozoic basalts in Hainan Island, SE Asia: a consequence of a young thermal mantle plume close to subduction zones? *Journal of Petrology,* 53(1):177–233. **http://dx.doi.org/10.1093/petrology/egr061**

Wang, Y., and Yang, Q., 1992. Neogene and Quaternary radiolarians from Leg 125. *In* Fryer, P., Pearce, J.A., Stokking, L.B., et al., *Proceedings of the Ocean Drilling Program, Scientific Results,* 125: College Station, TX (Ocean Drilling Program), 95–112. **http://dx.doi.org/10.2973/odp.proc.sr.125.174.1992**

Wetzel, A., 2009. The preservation potential of ash layers in the deep-sea: the example of the 1991-Pinatubo ash in the South China Sea. *Sedimentology,* 56(7):1992–2009. **http://dx.doi.org/10.1111/j.1365-3091.2009.01066.x**

Wetzel, A., and Unverricht, D., 2013. A muddy megaturbidite in the deep central South China Sea deposited ~350 yrs BP. *Marine Geology,* 346:91–100. **http://dx.doi.org/10.1016/j.margeo.2013.08.010**

Zhang, G., Smith-Duque, C., Tang, S., Li, H., Zarikian, C., D'Hondt, S., Inagaki, F., and IODP Expedition 329 Scientists, 2012a. Geochemistry of basalts from IODP Site U1365: implications for magmatism and mantle source signatures of the mid-Cretaceous Osbourn Trough. *Lithos,* 144–145:73–87. **http://dx.doi.org/10.1016/j.lithos.2012.04.014**

Zhang, G., Zeng, Z., Yin, X., Wang, X., and Chen, D., 2009. Deep fractionation of clinopyroxene in the East Pacific Rise 13°N: evidence from high MgO MORB and melt inclusions. *Acta Geologica Sinica,* 83(2):266–277. **http://dx.doi.org/10.1111/j.1755-6724.2009.00030.x**

Zhang, G.-L., Chen, L.-H., and Li, S.-Z., 2013. Mantle dynamics and generation of a geochemical mantle boundary along the East Pacific Rise—Pacific/Antarctic Ridge. *Earth and Planetary Science Letters,* 383:153–163. **http://dx.doi.org/10.1016/j.epsl.2013.09.045**

Zhang, G.-L., Zong, C.-L., Yin, X.-B., and Li, H., 2012b. Geochemical constraints on a mixed pyroxenite–peridotite source for East Pacific Rise basalts. *Chemical Geology,* 330–331:176–187. **http://dx.doi.org/10.1016/j.chemgeo.2012.08.033**

Zijderveld, J.D.A., 1967. AC demagnetization of rocks: analysis of results. *In* Collinson, D.W., Creer, K.M., and Runcorn, S.K. (Eds.), *Methods in Palaeomagnetism:* Amsterdam (Elsevier), 254–286.